Mon. Not. R. Astron. Soc. **399,** 497–514 (2009) doi:10.1111/j.1365-2966.2009.15034.x

Substructures in hydrodynamical cluster simulations

K. Dolag,[1⋆] S. Borgani,[2,3,4⋆] G. Murante[5] and V. Springel[1]

[1]*Max-Planck-Institut für Astrophysik, Karl-Schwarzschild Strasse 1, Garching bei München, Germany*
[2]*Dipartimento di Astronomia dell'Università di Trieste, via Tiepolo 11, I-34131 Trieste, Italy*
[3]*INFN – Istituto Nazionale di Fisica Nucleare, Trieste, Italy*
[4]*INAF – Istituto Nazionale di Astrofisica, Trieste, Italy*
[5]*INAF – Astronomical Observatory of Torino, Str. Osservatorio 25, I-10025 Pino Torinese, Torino, Italy*

Accepted 2009 May 11. Received 2009 May 11; in original form 2008 August 25

Downloaded from https://academic.oup.com/mnras/article/399/2/497/1058378 by guest on 20 August 2022

ABSTRACT

The abundance and structure of dark matter subhaloes have been analysed extensively in recent studies of dark-matter-only simulations, but comparatively little is known about the impact of baryonic physics on halo substructures. We here extend the SUBFIND algorithm for substructure identification such that it can be reliably applied to dissipative hydrodynamical simulations that include star formation. This allows, in particular, the identification of galaxies as substructures in simulations of clusters of galaxies and a determination of their content of gravitationally bound stars, dark matter and hot and cold gas. Using a large set of cosmological cluster simulations, we present a detailed analysis of halo substructures in hydrodynamical simulations of galaxy clusters, focusing in particular on the influence both of radiative and non-radiative gas physics and of non-standard physics such as thermal conduction and feedback by galactic outflows. We also examine the impact of numerical nuisance parameters such as artificial viscosity parameterizations. We find that diffuse hot gas is efficiently stripped from subhaloes when they enter the highly pressurized cluster atmosphere. This has the effect of decreasing the subhalo mass function relative to a corresponding dark-matter-only simulation. These effects are mitigated in radiative runs, where baryons condense in the central subhalo regions and form compact stellar cores. However, in all cases, only a very small fraction, of the order of one per cent, of subhaloes within the cluster virial radii preserve a gravitationally bound hot gaseous atmosphere. The fraction of mass contributed by gas in subhaloes is found to increase with the cluster-centric distance. Interestingly, this trend extends well beyond the virial radii, thus showing that galaxies feel the environment of the pressurized cluster gas over fairly large distances. The compact stellar cores (i.e. galaxies) are generally more resistant against tidal disruption than pure dark matter subhaloes. Still, the fraction of star-dominated substructures within our simulated clusters is only $\sim$10 per cent. We expect that the finite resolution in our simulations makes the galaxies overly susceptible to tidal disruption, hence the above fraction of star-dominated galaxies should represent a lower limit for the actual fraction of galaxies surviving the disruption of their host dark matter subhalo.

Key words: hydrodynamics – methods: numerical – galaxies: clusters: general – galaxies: evolution – cosmology: theory.

1 INTRODUCTION

The hierarchical cold dark matter (CDM) model has been established as the standard model of cosmic structure formation, and its parameters are now tightly constrained by a variety of observations (e.g. Springel, Frenk & White 2006; Komatsu et al. 2009, and references therein). Within the CDM scenario, galaxy clusters are the largest gravitationally bound objects in the universe, and they exhibit rich information about the process of structure formation. As a result, they attract great interest from both observational and theoretical points of view. Due to their recent formation, clusters of galaxies also represent the ideal places where the hierarchical assembly of structures is 'caught in the act'. Indeed, the complexity of their internal structure reflects the infall of hundreds, if not thousands, of smaller objects and their subsequent destruction or

⋆E-mail: kdolag@mpa-garching.mpg.de (KD); borgani@oats.inaf.it (SB)

© 2009 The Authors. Journal compilation © 2009 RAS

survival within the cluster potential. The dynamical processes determining the fate of the accreting structures also provide the link between the internal dynamics of clusters and the properties of their galaxy population.

Modern cosmological simulations provide an ideal tool to study the non-linear dynamics of these processes in a cosmological environment. Thanks to the high resolution reached by dark matter (DM) only simulations, a consistent picture of the population of subhaloes within galaxy clusters has now emerged (Moore et al. 1999; Ghigna et al. 2000; Springel et al. 2001b; Stoehr et al. 2002, 2003; De Lucia et al. 2004; Diemand, Moore & Stadel 2004; Gao et al. 2004; Kravtsov et al. 2004). Although these simulations give a highly detailed description of the evolution of DM substructures, they cannot provide information on how gas-dynamical processes affect the properties and the dynamics of substructures. Yet, such an understanding is needed to make a more direct link of the properties of DM substructures with those of the galaxies that orbit in clusters. For example, we would like to know the time-scale over which subhaloes can retain their diffuse gas once they infall into a cluster, as this also determines the time interval over which gas can continue to cool and to refuel ongoing star formation. Being highly pressurized, the intracluster medium (ICM) is quite efficient in stripping gas from merging structures (Gunn & Gott 1972; see also McCarthy et al. 2008 and references therein), thereby altering both the mass of the subhaloes and their survival time. The stripping also governs the time-scale over which galaxy morphology and colours are modified inside galaxy clusters (Abadi, Moore & Bower 1999; Kenney, van Gorkom & Vollmer 2004). Finally, although baryons are expected to only play a subdominant role for the dynamics of substructures due to their limited mass fraction, they may nevertheless alter the structure of subhaloes in important ways, affecting their survival, mass-loss rate, abundance and radial distribution. Quantifying these differences relative to DM-only simulations is an important challenge for the present generation of cosmological hydrodynamical simulations.

So far, there have only been a limited number of investigations of the properties of subhaloes within hydrodynamical simulations. Based on cluster simulations with the adaptive mesh refinement code ART, Nagai & Kravtsov (2005) have demonstrated that the stellar mass of infalling galaxies is approximately conserved and the survival of the galaxies is slightly enhanced. Similar studies using the TREESPH code GASOLINE have been performed by Macciò et al. (2006), where twice as many subhaloes within the central part of a Galaxy-sized halo were found when compared with pure DM simulations. Finally, Weinberg et al. (2008) used a TREESPH code to investigate the halo occupation and subhalo correlation functions for one group-sized halo, also pointing out the enhanced survival of substructures in the hydrodynamical runs.

Here, we present a systematic analysis of a large sample of galaxy clusters, with an emphasis on the role of non-standard physics and the details of feedback prescriptions on the survival of galaxies. Additionally, we also present an analysis of the evolution of the diffuse gas within the galaxies. In general, our findings are in broad agreement with those in previous studies, but we stress that our star dominant systems are still not as numerous as expected from semi-analytic modelling *to reproduce the cluster luminosity functions* (*e.g. De Lucia & Blaizot 2007; see also Baugh 2006 for a review on semi-analytic models of galaxy formation)*.

Thanks to improvements in numerical codes and higher computer performance, cosmological hydrodynamical simulations of galaxy clusters can now model a number of the most important physical processes in galaxy formation, such as radiative cooling, star formation and feedback in energy and metals, while at the same time reaching sufficient resolution to treat these processes in a numerically robust and physically meaningful way (e.g. Borgani et al. 2008, for a recent review). This allows more realistic structure formation calculations of the coupled system of DM and baryonic gas than possible with DM-only simulations, far into the highly non-linear regime. For instance, radiative cooling has the effect of letting a significant fraction of the baryons cool at the halo centres, which alters the shape and concentration of haloes through the mechanism of adiabatic contraction (e.g. Gnedin et al. 2004). At the same time, the condensation of cooled baryons and their subsequent conversion into collisionless stars are expected to largely protect them from stripping, reducing the rate of disruption of substructures and increasing their survival times. Indeed, assuming that galaxies at least survive for a while the disruption of their host DM haloes has been shown to be crucial for semi-analytical models (SAMs) of galaxy formation to provide a successful description of the observed galaxy population in clusters (e.g. Gao et al. 2004).

This discussion highlights the importance of understanding the properties and the evolution of cluster substructures as predicted by modern cosmological hydrodynamical simulations. Evidently, an important technical prerequisite for such an analysis is the availability of suitable numerical algorithms to reliably identify substructure in dissipative simulations. To this end, we introduce a modified version of the SUBFIND algorithm, and test its robustness. We then apply it in a detailed analysis of the properties of substructures in a large ensemble of galaxy clusters, which have been simulated at different resolutions both in their DM-only version and in several further versions where different physical processes were included, such as non-radiative and radiative hydrodynamics, star formation, energy feedback, gas viscosity and thermal conduction. The aim of this analysis is to quantify the numerical robustness of the measured properties of substructures, and to identify the quantitative influence of these physical processes on substructure statistics in comparison with DM-only models.

The paper is organized as follows. We describe in Section 2 the sample of galaxy clusters and the simulations performed. Section 3 provides a description of the algorithm used to identify gravitationally bound substructures. This algorithm is a modified version of SUBFIND (Springel et al. 2001b), which we suitably changed to allow extraction of bound structures from *N*-body/smoothed particle hydrodynamics (SPH) simulations also in the presence of gas and star particles. In Section 4, we present our results about the properties of the substructures in both DM and hydrodynamical simulations. We summarize our results and outline our main conclusion in Section 5. An Appendix is devoted to the presentation of tests of resolution and numerical stability of our analysis.

2 SIMULATIONS

In this section, we describe our set of simulated clusters, the different physical processes we considered and the numerical choices made for the different runs.

2.1 Simulated physics

The simulations were carried out with the TREEPM/SPH code GADGET-2 (Springel, White & Hernquist 2001a; Springel 2005), which makes use of the entropy-conserving formulation of SPH (Springel & Hernquist 2002). Some of our non-radiative simulations were carried out with different implementations of artificial viscosity compared with the standard one in GADGET-2, however, which allows us

Downloaded from https://academic.oup.com/mnras/article/399/2/497/1058378 by guest on 20 August 2022

to investigate the effect of numerical viscosity on the stripping of gas from substructures within galaxy clusters. In Dolag et al. (2005), it was shown that the amount of turbulence detectable within the cluster atmosphere is quite sensitive to the numerical treatment of the artificial viscosity, so one expects that the stripping of the gas from substructures might also be affected by these numerical details. In the following, we will label simulations that use the original parametrization of the artificial viscosity by Monaghan & Gingold (1983) and Balsara (1995) as OVISC. This was found to be the scheme with the highest numerical viscosity in the study of Dolag et al. (2005). An alternative formulation with slightly less numerical viscosity is based on the signal velocity approach of Monaghan (1997), and is labelled as SVISC. Finally, we considered a modified artificial viscosity scheme as originally suggested by Morris & Monaghan (1997), labelled as LVISC. In this scheme, every particle evolves its own time-dependent viscosity parameter, with the goal to only have high viscosity in regions where it is really needed. In this scheme, shocks are generally as well captured as in the standard approach, but regions away from the shocks experience less artificial viscosity, such that an inviscid ideal gas is represented more faithfully. As a result, turbulence driven by fluid instabilities can be better resolved, and simulated galaxy clusters are able to build up a higher level of turbulence generated along the shear flows arising in the cosmological structure formation process (see Dolag et al. 2005).

GADGET-2 also includes, if enabled, radiative cooling, heating by a uniform redshift-dependent ultraviolet background (Haardt & Madau 1996) and a treatment of star formation and feedback processes. Simulations that account for radiative cooling and star formation allow us to study the effect of a compact stellar core at the centre of substructures on subhalo survival and disruption. The prescription of star formation we use is based on a subresolution model to account for the multiphase structure of the interstellar medium (ISM), where the cold phase of the ISM is the reservoir of star formation (Springel & Hernquist 2003). Supernovae (SNe) heat the hot phase of the ISM and provide energy for evaporating some of the cold clouds, thereby leading to self-regulation of the star formation and an effective equation of state for describing its dynamics.

As a phenomenological extension of this feedback scheme, Springel & Hernquist (2003) also included a simple model for galactic winds, whose velocity, v_w, scales with the fraction η of the Type II SN feedback energy that contributes to the winds. The total energy provided by Type II SN is computed by assuming that they are due to exploding massive stars with mass $>8\,M_\odot$ from a Salpeter (1955) initial mass function (IMF), with each SN releasing 10^{51} ergs of energy. In our simulations with winds, we will assume $\eta = 0.5$ and 1, yielding $v_w \simeq 340$ (CSF) and 480 km s^{-1} (CSFSW), respectively, while we will also explore the effect of switching off galactic winds (CSFNW). We refer to Table 1 for a schematic description and overview of the physical and numerical schemes included in our simulations.

For some of our cluster simulations, we also included the effect of heat conduction (CSFC), based on the implementation described by Jubelgas, Springel & Dolag (2004). In the simulations presented

Table 1. Symbolic names of the different runs analysed here, together with a short description of the physical processes included, and references to studies that used the simulations previously or that give specific details for the physical models used. For each physical model, we also specify for which cluster the simulations have been carried out.

Name	Included physics	Reference	Used in
DM-only			
dm	Gravity	–	Puchwein et al. (2005), Giocoli, Tormen & van den Bosch (2008), Meneghetti et al. (2007, 2008)
(*g676*, *g914*,*g1542*, *g3344*,*g6212*, *g1*, *g8*,*g51*, *g72* and *g696*)			
Non-radiative runs			
OVISC	Usual parametrization of artificial viscosity	Dolag et al. (2005)	Puchwein et al. (2005), Ettori et al. (2006), Dolag et al. (2006), Bonaldi et al. (2007), Cora et al. (2008), Puchwein & Bartelmann (2006, 2007), Meneghetti et al. (2007)
(*g676*, *g914*,*g1542*, *g3344*,*g6212*, *g1*, *g8*,*g51*, *g72* and *g696*)			
SVISC	Artificial viscosity based on signal velocity	Dolag et al. (2005)	
(*g676*, *g914*,*g1542*, *g3344*,*g6212*, *g1*, *g8*,*g51* and *g72*)			
LVISC	Time varying, low-artificial-viscosity scheme	Dolag et al. (2005)	Ettori et al. (2006), Vazza et al. (2006)
(*g676*, *g914*,*g1542*, *g3344*,*g6212*, *g1*, *g8*,*g51* and *g72*)			
Cooling, star-formation and thermal feedback			
CSFNW	No winds	–	Ettori et al. (2006), Borgani et al. (2006)
(*g676* and *g51*)			
CSF	Weak winds ($v_w = 340$km/h)	–	Puchwein et al. (2005), Rasia et al. (2005), Ettori et al. (2006), Bonaldi et al. (2007), Borgani et al. (2006), Ameglio et al. (2006, 2007)
(*g676*, *g914*,*g1542*, *g3344*,*g6212*, *g1*, *g8*,*g51*, *g72* and *g696*)			
CSFSW	Strong winds ($v_w = 480$km/h)	–	Ettori et al. (2006), Borgani et al. (2006)
(*g676* and *g52*)			
CSFC	Weak winds ($v_w = 340$ km/h) and thermal conduction ($\kappa = 0.3$)	Dolag et al. (2004b)	Ettori et al. (2006), Rasia et al. (2006), Bonaldi et al. (2007)
(*g676*, *g914*,*g1542*, *g3344*,*g6212*, *g1*, *g8*,*g51*, *g72* and *g696*)			

Downloaded from https://academic.oup.com/mnras/article/399/2/497/1058378 by guest on 20 August 2022

here, we assume an isotropic effective conductivity parametrized as a fixed fraction of 1/3 the *Spitzer* rate. We also account for saturation, which can become relevant in low-density gas and at the interface between cold and hot media. We refer to Dolag et al. (2004b) for more details on the effect of thermal conduction on the thermodynamical properties of the ICM.

2.2 The set of simulated clusters

The clusters analysed in this study are extracted from 10 resimulations of Lagrangian regions selected from a cosmological lower resolution DM-only simulation (Yoshida, Sheth & Diaferio 2001). This parent simulation has a box size of $479\,h^{-1}$ Mpc, and assumed a flat ΛCDM cosmology with $\Omega_{\rm m} = 0.3$ for the matter density parameter, $H_0 = 70\,{\rm km\,s^{-1}\,Mpc^{-1}}$ for the Hubble constant, $f_{\rm bar} = 0.13$ for the baryon fraction and $\sigma_8 = 0.9$ for the normalization of the power spectrum. As such, the values of $\Omega_{\rm m}$ and σ_8 in this model are somewhat higher than the best-fitting values obtained from the analysis of the 5-year *Wilkinson Microwave Anisotropy Probe* data (Dunkley et al. 2009), but are still consistent with the current cosmological constraints.

Five of the regions have been selected to surround low-mass clusters ($m_{\rm cluster} \approx 10^{14}\,{\rm M}_\odot$), while four other regions surround massive ($m_{\rm cluster} \gtrsim 10^{15}\,{\rm M}_\odot$) clusters. Besides the central massive cluster, three of these four regions also contain 12 additional smaller clusters, all having virial masses above $10^{14}\,{\rm M}_\odot$. The tenth simulated region surrounds a filamentary structure which includes four massive ($m_{\rm cluster} > 10^{15}\,{\rm M}_\odot$) clusters (see Dolag et al. 2006). Ray-tracing images, obtained with the SPLOTCH package (Dolag et al. 2008), of the gas temperature for the simulated cluster regions are shown in Fig. 1. Besides giving an impression of the complexity and the dynamics of the ICM within the simulated galaxy clusters, this figure also highlights a couple of interesting key features of hydrodynamical cluster simulations. The white colours in general correspond to high density, whereas the red colour marks the hot, shock-heated atmosphere of the cluster. The transition to the unshocked material (mainly indicated by the blue colour) is clearly visible and indicates the location of the accretion shocks, which for clusters at redshift zero are typically at much larger distances than the virial radius (see Table 2). Also clearly visible are denser and colder filaments that penetrate the hot cluster atmosphere. Many of the gaseous haloes of the substructures show comet-like features, a telltale sign of gas being stripped. Sometimes this happens already at relatively large distances from the cluster centre, demonstrating a change in the environment that becomes important already at distances of several virial radii (e.g. Dolag et al. 2006).

Using the 'zoomed initial conditions' technique (Tormen, Bouchet & White 1997), these regions were resimulated with higher mass and force resolution by populating their Lagrangian volumes with a larger number of particles, while appropriately adding additional high-frequency modes drawn from the same power spectrum. To optimize the setup of the initial conditions, the high-resolution region was sampled with a 16^3 grid (for the more massive systems even with a 64^3 grid), where only subcells are resampled at high resolution to allow for nearly arbitrary shapes of the high-resolution region. The exact shape of each final high-resolution region was iteratively obtained by repeatedly running DM-only simulations until the target objects were free of any contamination by lower resolution boundary particles out to 3–5 virial radii. The initial unperturbed particle distribution (before imprinting the Zeldovich displacements) was realized through a relaxed glass-like configuration (White 1996).

Gas was then added to the high-resolution regions by splitting each parent particle into a gas and a DM particle. The gas and the DM particles were displaced by half of the original mean interparticle distance, such that the centre of mass and the momentum of the original particle are conserved. As a further optimization to save CPU time, the splitting of the DM particles in our largest simulations (i.e. those of the filamentary structure) was applied only to a subset of the high-resolution particles, selected by the following procedure. Instead of defining the high-resolution region with the help of a grid, we used a surface around the centre of the high-resolution region. For this purpose, we pixelized a fiducial sphere around the centre of the high-resolution region using 4×16^2 pixels, making use of the HEALPIX tessellation of the full sky (Górski, Hivon & Wandelt 1998), which has the advantage of offering an equal solid angle covered by each pixel. We then traced back in Lagrangian space all the particles in the DM-only run which at $z = 0$ end up within 5 virial radii of the four massive clusters. All such particles were then projected on to the spherical coordinate system, where we recorded the maximum distance within each pixel of our HEALPIX representation. In a second step, all particles within the high-resolution region were projected on to the spherical coordinate system and only those with distances smaller than the recorded maximum distance of the corresponding pixel of our HEALPIX representation were then marked to define the region where to add gas. This optimization procedure reduced the number of gas particles by about 40 per cent, without significantly reducing the size of the regions around the target objects where hydrodynamics are correctly computed.

The final mass resolution of the gas particles in our simulations is $m_{\rm gas} = 2.4 \times 10^8\,{\rm M}_\odot$. Thus, the massive clusters were resolved with between 2×10^6 and 4×10^6 particles. In all simulations, the gravitational softening length was kept fixed at $\epsilon = 42\,{\rm kpc}$ comoving Plummer equivalent, and was switched to a physical softening length of $\epsilon = 7\,h^{-1}$ kpc at $z = 5$.

The high-resolution regions around the massive clusters are quite large and therefore also include other lower mass systems, which are still free of contamination from low-resolution particles. Hence, these systems can be included in our analysis. In this way, we end up with a total sample of 25 clusters having a mass of at least $10^{14}\,{\rm M}_\odot$. The basic characteristics of these cluster, such as masses and radii at different overdensities, both for the DM-only runs and for the non-radiative OVISC runs, are given in Table 2.

To study resolution effects in the substructure mass distribution in the DM runs, we also performed all these simulations at six times higher mass resolution, with the gravitational softenings decreased accordingly by a factor of $6^{1/3} \simeq 1.8$. In the following, we refer to these simulations as our high-resolution DM runs.

Finally, In Appendix A we will show results of a resolution study of one cluster, taken from a different set of cluster simulations (Borgani et al. 2006), which has been simulated at three different resolution. In the same Appendix, we will also discuss the effect of adding gas particles in the initial conditions in such a way that there are eight times fewer gas particles, but each having roughly the mass as that of the high-resolution DM particles.

3 DETECTION OF SUBSTRUCTURES

Substructures within haloes are usually defined as locally overdense, self-bound particle groups identified within a larger parent halo. In our analysis, the identification of these substructures is performed by applying the SUBFIND algorithm (Springel et al. 2001b), which is defined in its original form only for DM-only simulations. In brief, as a first step, we employ a standard friends-of-friends (FoF)

Downloaded from https://academic.oup.com/mnras/article/399/2/497/1058378 by guest on 20 August 2022

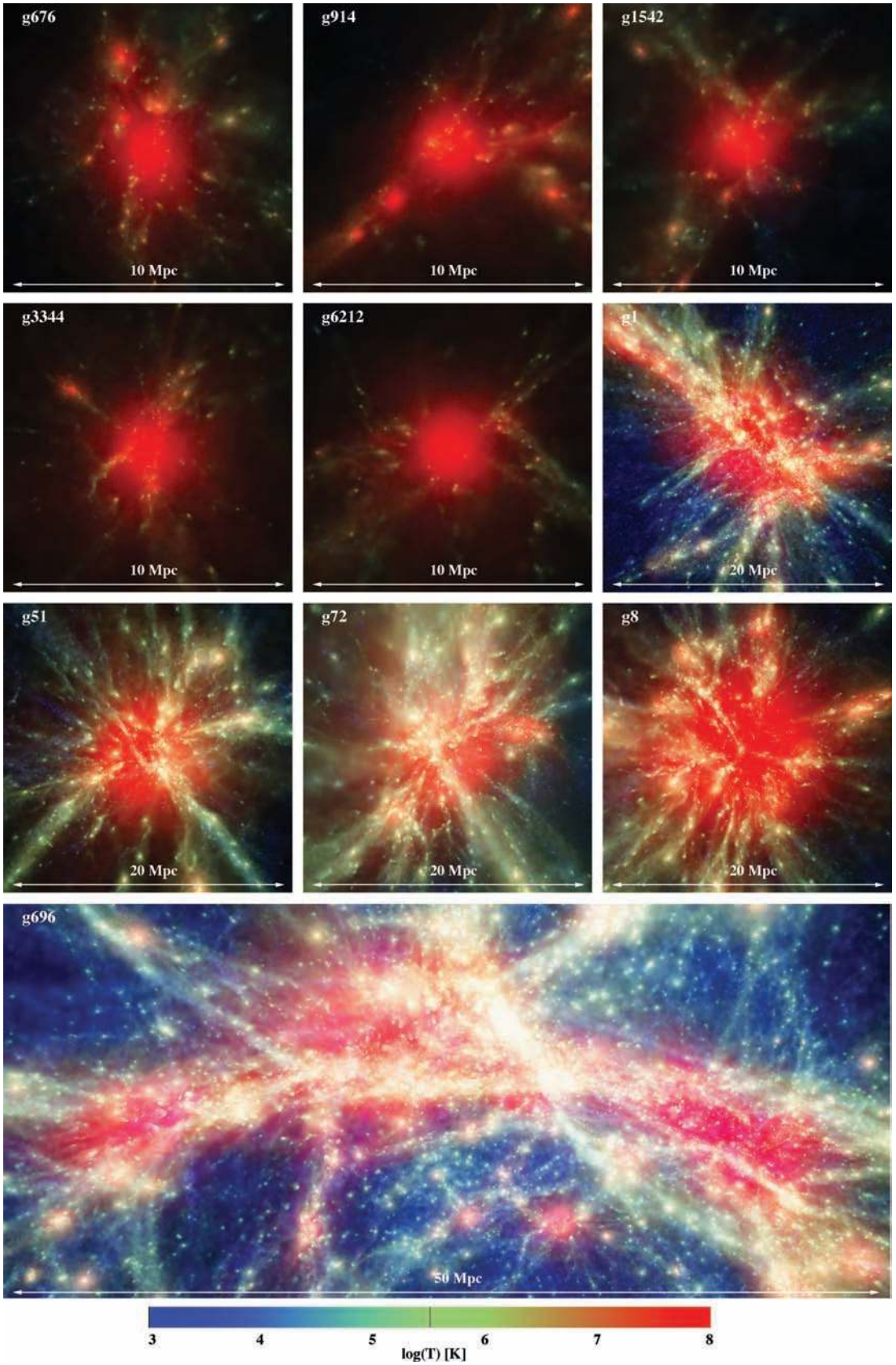

Figure 1. Visualization of the gas temperature in the non-radiative (OVISC) simulations of the 10 clusters discussed in the text, carried out with the ray-tracing software SPLOTCH. An animation flying through one of the simulated clusters can be downloaded from http://www.mpa-garching.mpg.de/galform/data_vis/index.shtml#movie9.

Downloaded from https://academic.oup.com/mnras/article/399/2/497/1058378 by guest on 20 August 2022

Table 2. General properties of the simulated clusters at $z = 0$ for the cases of DM-only runs (left-hand part of the table) and for the OVISC version of the non-radiative runs (right-hand part of the table).

	dm						OVISC					
Cluster	$R_{\rm vir}$	$M_{\rm vir}$	R_{200}	M_{200}	R_{500}	M_{500}	$R_{\rm vir}$	$M_{\rm vir}$	R_{200}	M_{200}	R_{500}	M_{500}
g676.a	1.43	1.60	1.07	1.39	0.71	1.06	1.40	1.53	1.06	1.33	0.71	1.03
g914.a	1.50	1.84	1.09	1.44	0.71	1.06	1.46	1.73	1.09	1.43	0.71	1.06
g1542.a	1.40	1.53	1.043	1.29	0.69	0.93	1.40	1.53	1.043	1.30	0.69	0.94
g3344.a	1.44	1.64	1.07	1.40	0.73	1.10	1.43	1.63	1.07	1.39	0.73	1.07
g6212.a	1.43	1.61	1.06	1.33	0.70	1.00	1.43	1.61	1.06	1.31	0.70	1.00
g51.a	3.26	19.21	2.39	15.33	1.56	10.66	3.26	19.03	2.37	15.30	1.57	11.16
g72.a	3.29	19.63	2.40	15.59	1.57	10.93	3.29	19.63	2.37	15.29	1.59	11.20
g72.b	1.71	2.81	1.21	2.03	0.71	1.04	1.71	2.79	1.26	2.24	0.74	1.19
g1.a	3.40	21.86	2.54	18.86	1.73	14.61	3.37	21.16	2.50	17.80	1.69	13.59
g1.b	2.31	6.83	1.64	5.07	1.04	3.26	2.26	6.43	1.67	5.36	1.06	3.43
g1.c	1.67	2.61	1.23	2.09	0.79	1.40	1.69	2.66	1.23	2.09	0.79	1.41
g1.d	1.60	2.29	1.10	1.53	0.63	0.71	1.57	2.14	1.07	1.40	0.61	0.66
g1.e	1.27	1.14	0.94	0.94	0.59	0.56	1.26	1.10	0.93	0.93	0.63	0.70
g1.f	1.14	0.81	0.77	0.53	0.49	0.34	1.11	0.77	0.77	0.53	0.50	0.34
g8.a	3.90	32.70	2.86	26.63	1.90	19.64	3.94	33.87	2.89	27.56	1.93	20.60
g8.b	1.50	1.86	1.09	1.44	0.69	0.93	1.54	2.01	1.14	1.70	0.74	1.20
g8.c	1.36	1.37	0.93	0.93	0.60	0.60	1.43	1.61	1.03	1.24	0.61	0.66
g8.d	1.34	1.34	0.89	0.80	0.59	0.56	1.40	1.51	1.00	1.14	0.66	0.81
g8.e	1.30	1.23	0.96	1.00	0.60	0.61	1.33	1.30	0.96	1.00	0.63	0.69
g8.f	1.14	0.83	0.83	0.66	0.46	0.29	1.20	0.94	0.87	0.76	0.54	0.47
g8.g	1.11	0.76	0.77	0.53	0.47	0.31	1.06	0.66	0.76	0.49	0.50	0.36
g696.a	3.26	19.07	2.40	15.79	1.56	10.81	3.24	18.94	2.39	15.51	1.57	11.00
g696.b	3.13	17.04	2.23	12.64	1.43	8.23	3.19	17.87	2.29	13.51	1.47	9.10
g696.c	2.79	11.97	2.07	10.04	1.27	5.81	2.77	11.87	2.07	10.13	1.29	6.06
g696.d	2.67	10.57	1.83	7.04	1.14	4.30	2.59	9.51	1.81	6.80	1.14	4.29

Note. Column 1: cluster names; Columns 2 (7) and 3 (8): virial radii (in units of Mpc) and virial masses (in units of $10^{14}\,{\rm M}_{\odot}$); Columns 5 (10) and 4 (9): masses contained within the radius R_{200}, encompassing an average density of $200\,\rho_{\rm crit}$ and values of R_{200}; Columns. 7 (12) and 6 (11): the same as before, but referring to a mean density of $500\,\rho_{\rm crit}$.

algorithm to identify the parent haloes. In our analysis, we have used a FoF linking length of 0.16 times the mean DM particle separation. Note that this linking length is obtained when scaling the *standard* linking length of 0.2 by $(\Delta_c/\Omega)^{-1/3}$ according to the adopted cosmology and leads to groups having the overdensity characteristic of virialized objects predicted by the spherical collapse model (see Eke, Cole & Frenk 1996). The density of each particle within a FoF group is then estimated by adaptive kernel interpolation, using the standard SPH approach with a certain number of neighbouring particles. Using an excursion set approach where a global density threshold is progressively lowered, we find locally overdense regions within the resulting density field, which form a set of substructure candidates. The outer 'edge' of the substructure candidate is determined by a density contour that passes through a saddle point of the density field; here, the substructure candidate joins on to the background structure. In a final step, all substructure candidates are subjected to a gravitational unbinding procedure where only the self-bound part is retained. If the number of bound particles left is larger than a prescribed minimum detection threshold, we register the substructure as genuine *subhalo*.

For full details on this substructure-finding algorithm as applied to DM-only simulations, we refer the reader to the paper by Springel et al. (2001b). In the following, we briefly describe the modifications to the algorithm that we implemented in order to make it applicable to simulations which also contain gas and star particles.

Because the DM particles and the baryonic particles are in general distributed differently (especially in simulations with cooling), it is problematic to apply the FoF algorithm to all particles at once on an equal footing. This would not select groups that are bounded by a clearly defined density contour, and produces systematic biases in the relative mass content of baryons and DM. We therefore apply the FoF only to the DM component of a simulation, using the same linking length that would be applied in a corresponding DM-only run. This selects haloes that are bounded at approximately the same DM overdensity contour, independent of the presence or absence of baryonic physics. Each gas and star particle is then associated with its nearest DM particle, i.e. if this DM particle belongs to a FoF group, then the corresponding baryonic particle is also associated with that group. This effectively encloses all baryonic material as part of a FoF group that is contained in the original DM overdensity contour.

We only keep FoF groups containing at least 32 DM particles for further analysis. Because a significant fraction of such small DM haloes are spurious, it is better to impose the detection limit just on the DM particle number and not on the total number or total FoF group mass, because the latter would boost the number of spurious substructures detected in hydrodynamical runs. Also, this limit ensures that the halo number densities detected in DM-only and in hydrodynamic runs should only differ because of the effects of the baryonic component on the DM dynamics, and not because of a change in the group detection procedure.

The second adjustment we made in SUBFIND is the procedure for density estimation in the presence of further components besides DM. We address this by first estimating the densities contributed by DM, gas particles and star particles at a given point separately for each of the components and then adding them up, i.e. the density

Downloaded from https://academic.oup.com/mnras/article/399/2/497/1058378 by guest on 20 August 2022

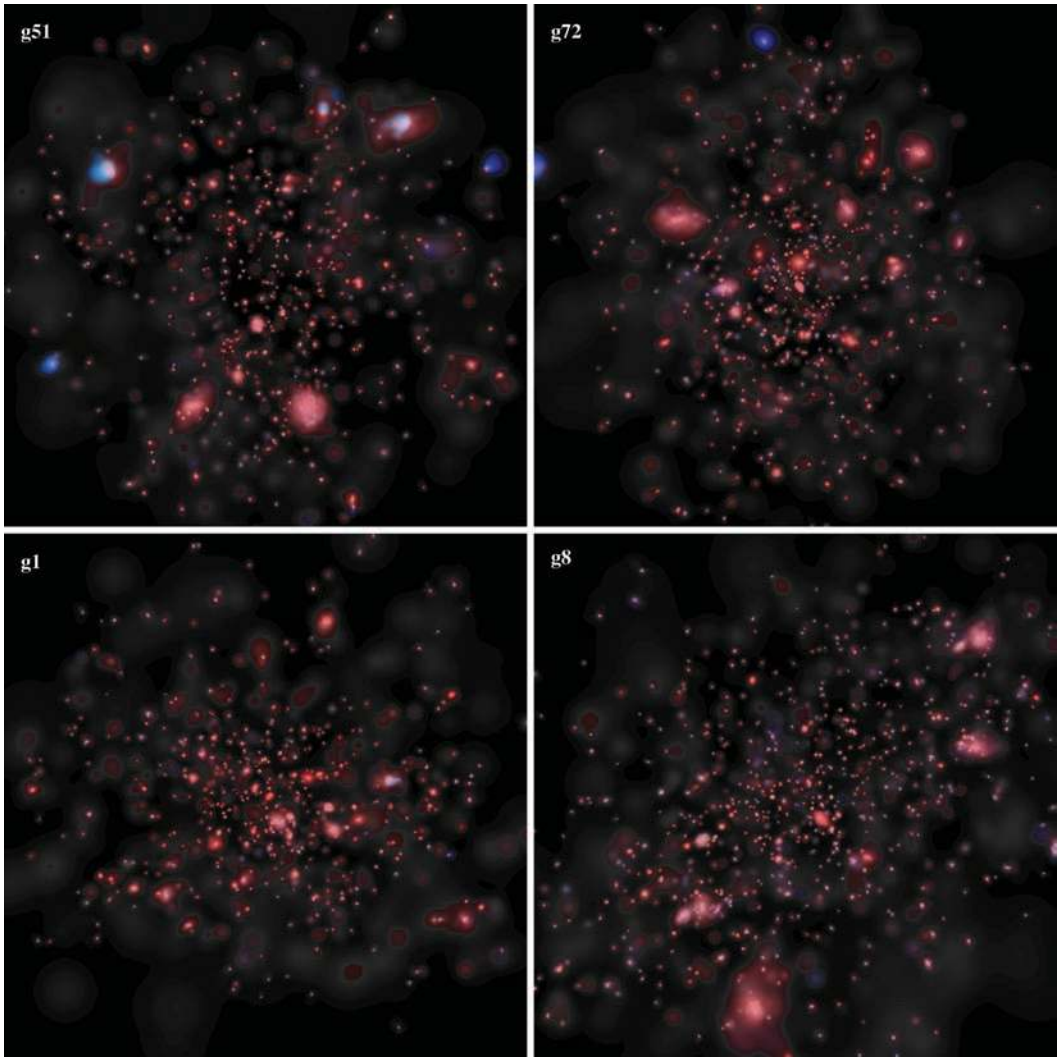

Figure 2. Visualization of all the identified galaxies within the virial radius of the g51, g72, g1 and g8 clusters (from top-left to bottom-right panels), simulated with cooling and star formation and galactic winds (CSF). About 1000 galaxies are identified within the virial radius of each of these massive clusters. Only the self-bound gas and star particles within substructures are included in the visualization, therefore excluding the hot atmosphere of the cluster and both the diffuse intracluster stellar population and the stars associated with the BCG. The colours of the stars represent their age, using a red to light blue colour table for decreasing age. Only a few of these galaxies, about 5–10 per cluster, still carry a self-bound hot gas halo, and those are located in the cluster peripheries. In the visualization, they appears as dark blue, extended haloes, often with a comet-like shape, stretched away from the galaxies.

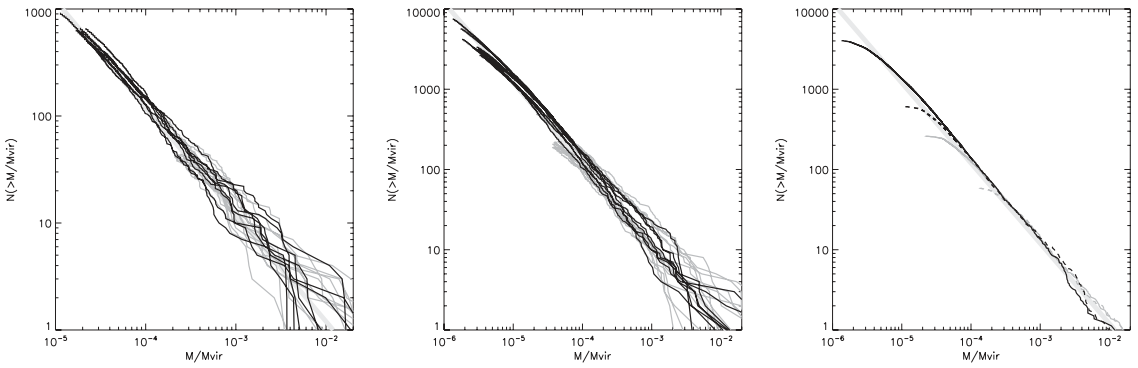

Figure 3. The cumulative subhalo mass functions for the DM runs of our clusters, normalized to the virial mass of each cluster. Left-hand panel: comparison between the 13 low-mass haloes (in grey) and the eight high-mass haloes (in black). Central panel: the same as in the left-hand panel, but for the runs with six times higher mass resolution. Right-hand panel: the average cumulative subhalo mass function for the low (in grey) and high (in black) mass sample from the DM-only runs. The dashed lines are for the simulations at the standard resolution while the solid lines are for the higher resolution runs. The corresponding best-fitting values of the power-law fit to each of these curves are given in Table 3. For reference, the grey thick line marks a power law with slope −1.

© 2009 The Authors. Journal compilation © 2009 RAS, MNRAS **399,** 497–514

Downloaded from https://academic.oup.com/mnras/article/399/2/497/1058378 by guest on 20 August 2022

carried by each of the three species is computed with the SPH kernel interpolation technique for neighbouring particles of the same species only. Again, this is done to avoid possible systematic biases in the density estimates. If they are done with all particles at once, the different particle masses and spatial distributions of the particle types can introduce comparatively large errors, for example when a few heavy DM particles dominate the sum over neighbours that mostly consist of light star particles. We note that we have carried out all the density computations with 32 neighbours.

Typically, the density contribution from the gas component is slightly smoother than that from the DM component (thanks to the gas pressure), whereas star particles generally trace a highly concentrated density field, thus making it easier to detect substructures dominated by star particles. As a net result, we find that the resulting total density field is a bit more noisy than the density field in pure DM runs. This led us to slightly modify SUBFIND's procedure to detect saddle points in the density field, and hence substructure candidates. In the default version of the algorithm, this is done by looking at the nearest two particles of a point that is added to the density field. We changed this to the nearest three points, finding that this leads to a significant improvement of the robustness of the identification of substructures in dissipative simulations while not changing the behaviour of the algorithm in pure DM or non-radiative runs.

Finally, as a further refinement in SUBFIND, we take into account the internal thermal energy of the gas particles in the gravitational unbinding procedure. After unbinding, we keep substructures in our final list of subhaloes if they contain a minimum of 20 DM *and* star particles. We ignore gas particles in this detection threshold in order to avoid the detection of spurious gravitationally bound gas clumps. In principle, a cleaner mass threshold for detection would also be obtained by ignoring the star particle count for this validation, but including them also allows us to identify very low-mass systems that are dominated by the stellar component as genuine self-bound substructures. Since stars form at the bottom of the potential wells and are highly concentrated relative to the other two components, we find this does not produce a significant component of spurious subhaloes.

For each of the FoF groups that correspond to a cluster, we obtain in this way a catalogue of gravitationally bound subhaloes that in general contain a mixture of DM, star and gas particles. The centre of each subhalo is identified with the minimum of the gravitational potential occurring among the member particles. Similarly, for the cluster as a whole, we determine a suitable centre as the position of the particle that has the minimum gravitational potential. Around this point, we calculate the virial radius and mass with the spherical-overdensity approach, using the overdensity predicted by the generalized spherical top-hat collapse model (e.g. Eke et al. 1996). We define as subhaloes of a cluster all the substructures which are identified within its spherical virial radius. Note that this can sometimes include subhaloes that belong to a FoF group different from that of the main halo, due to the aspherical shapes of the FoF groups. Likewise, not all of the subhaloes in the cluster's FoF group are necessarily inside its virial radius.

4 SUBHALOES IN GALAXY CLUSTERS

4.1 DM-only simulations

As a first step, we characterize the mass distribution of subhaloes for the DM runs and check the effect of the mass of the parent halo and of resolution. For this purpose, we split our sample of simulated clusters into a high-mass sample, containing eight haloes with virial masses above $10^{15}\,\mathrm{M}_{\odot}$, and a low-mass sample, containing 13 haloes with masses ranging between $\approx 1.0 \times 10^{14}$ and $3.0 \times 10^{14}\,\mathrm{M}_{\odot}$ (see Table 1).

Fig. 3 shows the cumulative subhalo mass function, normalized to the virial mass of the clusters (i.e. subhalo masses are measured in units of the virial mass of the parent halo). In the left-hand central panels, the lines are for individual clusters, with grey and black lines showing the low-mass and high-mass samples, respectively. The scatter among different clusters is substantial for substructure counts below $\lesssim 100$, which only includes the most massive structures. However, once a few hundred substructures are considered, the abundance per unit virial mass becomes quite uniform. There appears to be no significant difference in the scatter of the high-mass end of the subhalo mass functions between our low- and high-mass cluster samples.

In the middle panel, we show the same results as in the left-hand panel, but now for six times higher mass resolution. This allows us to count down to subhaloes that are six times smaller in mass, yielding significantly higher total subhalo counts. There is no clear difference in the cluster-to-cluster scatter relative to the lower resolution simulations, suggesting that the scatter is not due to numerical noise but rather reflects the genuine variations in the abundance of massive subhaloes in different haloes.

This is corroborated by the right-hand panel of Fig. 3, where we compare the average mass functions for the two subsets of low- and high-mass clusters, and at the two numerical resolutions. The thick grey line marks a power law with slope of -1, for comparison. Clearly, the average slope of the subhalo mass function of both cluster samples and at both resolutions agrees perfectly.

This result is good in agreement with previous findings (e.g. De Lucia et al. 2004; Gao et al. 2004). However, unlike Gao et al. (2004), we here do not find a significant trend of the amplitude of the subhalo mass function as a function of halo mass, a result which is in line with the findings by De Lucia et al. (2004). However, it may simply be the relatively small range of halo masses probed by our simulations that prevents us from seeing the weak mass trend, despite the good resolution reached in our most massive systems. We note that in the high-resolution versions of the high-mass clusters, each main halo is resolved with more than 10 million DM particles within $R_{\rm vir}$, allowing several thousand subhaloes to be identified within each main halo.

A good quantitative fit to our measured subhalo mass functions can be obtained with a power-law of the form

$$N_m = N_{-4} \left(\frac{m_{\rm sub}/M_{\rm vir}}{\mathrm{M}_{\odot}} \right)^{\alpha}. \quad (1)$$

We obtain values of the slope α and of the normalization N_{-4} for each cluster by performing a fit to the numerical data above a lower limit of 100 DM particles (to be insensitive to the resolution limit) and for $m_{\rm sub}/M_{\rm vir} < 0.01$ (in order to reduce sensitivity to the scatter in the high-mass end of the subhalo mass function). The resulting fitting parameters are reported in Table 3, along with mean values over our cluster sample and the errors due to the object-by-object scatter. The results of this table confirm that at high resolution we obtain rather stable results for both the slope and the normalization of the subhalo mass functions. Furthermore, we find no significant differences between the mass functions of high- and low-mass clusters, both in slope and in normalization.

Downloaded from https://academic.oup.com/mnras/article/399/2/497/1058378 by guest on 20 August 2022

Table 3. The best-fitting parameters for the cumulative subhalo mass function of equation (1).

Cluster sample	N_{-4}	α
Low mass	141 ± 106	-1.01 ± 0.26
Low mass (high resolution)	131 ± 32	-0.97 ± 0.15
High mass	136 ± 17	-1.00 ± 0.07
High mass (high resolution)	142 ± 22	-0.99 ± 0.03

Note. Reported here are the values for the low- and high-mass samples of DM-only simulations. Results are shown for the simulations performed both at the standard and at the high resolution. Quoted errors correspond to the rms scatter computed among the best-fitting values obtained for the individual clusters.

4.2 Hydrodynamical runs

We now turn to an analysis of the subhalo mass functions in our hydrodynamical simulations. As described in Section 3, we have modified the subhalo detection algorithm SUBFIND such that it can properly take into account the presence of gas and star particles, besides the DM particles. Our modifications have been guided by the desire to avoid possible systematic biases due to the presence of multiple particle components, such that the final subhalo catalogues can be directly compared with those of a DM-only simulation, except that the subhaloes can now also contain gas and star particles.

Fig. 4 shows a comparison of the cumulative subhalo mass functions for the different runs we carried out for the high-mass *g51.a* cluster. The left-hand panel compares the total subhalo mass function for the DM-only run with three non-radiative hydrodynamic runs (solid lines) that used different treatments for the numerical viscosity (see Section 2.1 for details). Clearly, introducing non-radiative hydrodynamics causes a decrease of the total subhalo mass function by a sizable amount, and this is almost independent of the detailed scheme used for the artificial viscosity. If interpreted in terms of a shift in mass, the difference between the subhalo mass in the DM-only and in the gas runs *can be explained mostly by the high efficiency of gas removal during the infall of subhaloes into the cluster.* To demonstrate this, we increased the mass of each subhalo identified in the non-radiative run by an amount corresponding to the cosmic baryon fraction. If gas is completely stripped and this represents the only reason for the lower mass function then this correction should provide a mass function consistent with that of the corresponding DM run. *However,* the stripped mass cannot *completely* compensate for the mass difference between the DM and the non-radiative runs. *Besides removing gas, also their orbits are changed due to the effect of gas pressure* (*see also Tormen, Moscardini & Yoshida 2004; Puchwein et al. 2005; Saro et al. 2008*), *also with some indications that the remaining DM subhaloes might become easier to disrupt.*

The central panel of Fig. 4 shows the cumulative subhalo mass functions for the same cluster, but here comparing the DM run with the different radiative runs, which differ in the efficiency of the kinetic feedback (i.e. CSFNW, CSF and CSFSW), or in the presence of thermal conduction (i.e. CSFC). The bulk of gas cooling and subsequent star formation within subhaloes takes place before the galaxies are falling into the high-pressure environment of the ICM. Cooling has the effect of concentrating cold gas and therefore also collisionless stars forming out of the gas at the centres of these subhaloes. This increases the concentration of the mass distribution, and protects part of the baryonic mass from ram pressure stripping. As a result, the subhalo mass functions in these radiative runs increase when compared to the non-radiative cases and become quite similar to those of the DM-only runs, with only a marginal sensitivity to the adopted intensity of the feedback. Only in the run without any kinetic feedback (CSFNW), the resulting total subhalo masses are even slightly larger than for the DM runs. This is probably the consequence of the adiabatic contraction of the DM haloes, in response to the rather strong cooling taking place when galactic winds are turned off (e.g. Gnedin et al. 2004).

It is worth mentioning that the change of the disruption of subhaloes in the hydrodynamical simulations is due to a complex interplay between different processes. First, we find that the presence of baryons makes the underlying DM distribution more concentrated (see also Rasia, Tormen & Moscardini 2004; Lin et al. 2006). A further increase in the concentration of the DM profiles is also contributed by including radiative cooling. These findings are reported in the left-hand panel of Fig. 5, which shows the concentration parameter of DM profiles as a function of halo mass for all main haloes. The results for the DM (*dm*) runs are in good agreement with the fit originally presented by Dolag et al. (2004a). The concentrations in the non-radiative runs and in the runs with cooling and star formation increase on average by 3–8 per cent and by 10–25 per cent with

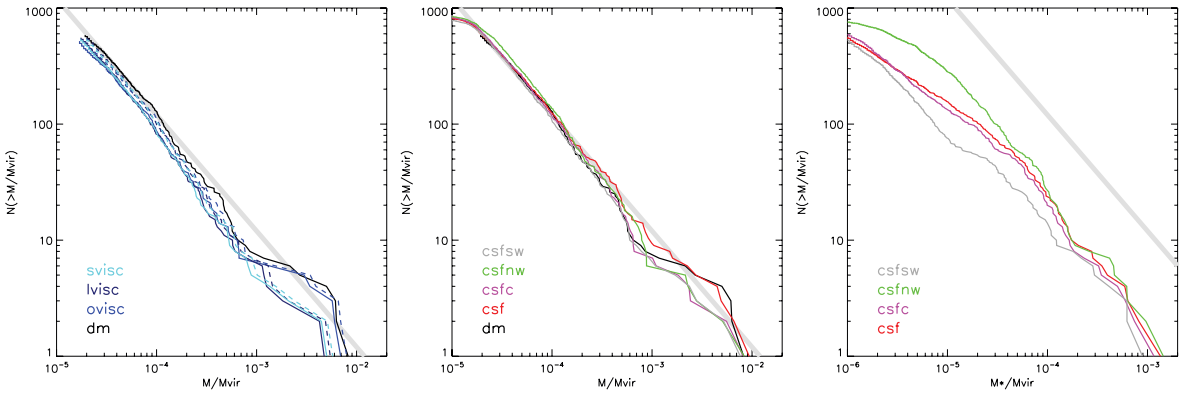

Figure 4. The cumulative total mass functions (left-hand and central panels) and stellar mass functions (right-hand panel) for the subhaloes identified in the *g*51 cluster at $z = 0$, as obtained for different runs. Left-hand panel: comparison of the total subhalo mass functions of the DM run with the non-radiative runs corresponding to different schemes for the artificial viscosity (solid lines). The dashed lines are obtained by correcting the mass of each subhalo in the non-radiative runs by increasing it by the cosmological baryon fraction. Central panel: the same as the left-hand panel, but for the different radiative runs. Right-hand panel: comparison between the stellar mass functions obtained for the different radiative runs. As in Fig. 3, the thick grey line marks a power-law with slope -1.

Downloaded from https://academic.oup.com/mnras/article/399/2/497/1058378 by guest on 20 August 2022

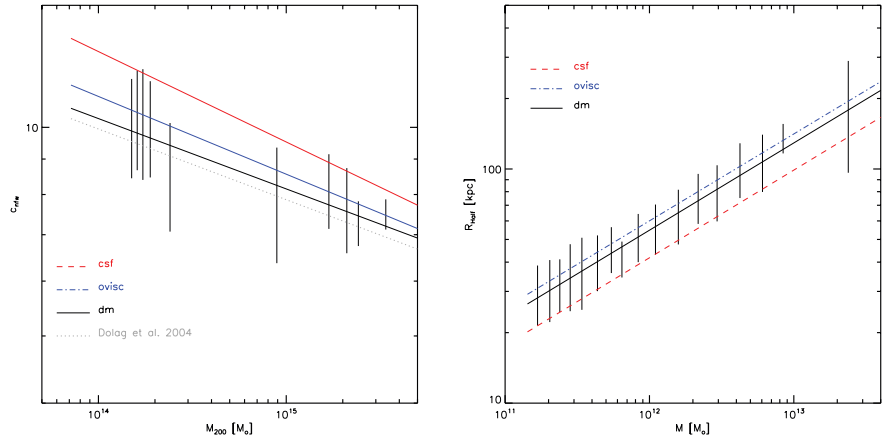

Figure 5. Left-hand panel: the concentration parameter, obtained by fitting a NFW profile (Navarro, Frenk & White 1996) to the DM density profiles in the hydrodynamical simulations, as a function of M_{200}. Here, we used all haloes with masses above $10^{14}\,M_{\odot}$ identified in all the simulation snapshots at redshift above $z = 0.5$, thereby scaling the obtained concentration parameter by $(1 + z)$ to compensate for the evolution. The different lines mark the results for the dark matter run (*dm*), the non-radiative run (OVISC) and the run with cooling and star formation (CSF). The dashed line gives the fit proposed in Dolag et al. (2004a). Right-hand panel shows the half-mass radius as a function of the subhalo mass for all substructures in all the clusters at redshift $z = 0$. The different lines distinguish the different simulations as before. In both panels, the error bars (shown only for the *dm* run) correspond to the rms scatter among all the clusters within each mass bin.

respect to the *dm* runs, respectively. The expectation based on this result is then that the haloes in the non-radiative runs are more difficult to destroy. However, as soon as the gas component is stripped from the subhaloes, the latter react to this mass loss with a slight expansion. In the non-radiative runs (OVISC), this expansion even slightly overcompensates the increase of the concentration. This is demonstrated by the right-hand panel of Fig. 5, which shows the half-mass radii of all substructures found in the main haloes at $z = 0$ as a function of their total mass. We find that this radius in the non-radiative runs (OVISC) is ≈2 per cent larger than in the pure *dm* runs. However, in the runs with cooling and star formation (CSF), the subhaloes remain more concentrated and we find the half-mass radius to be ≈5 per cent smaller than in the *dm* run. This increase in halo concentration is sufficient to compensate for the change of orbits due to the drag induced by the ram pressure (see Tormen et al. 2004; Puchwein et al. 2005; Saro et al. 2008). As a consequence, subhaloes survive for a longer time in the CSF runs, whereas these effects are nearly compensating in the non-radiative runs with a possible tendency for subhaloes to be more easily disrupted when compared to the *dm*-only runs.

For the radiative runs, we note that a small but sizable population of small subhaloes exists that are dominated by star particles and whose DM component was lost during the subhalo's evolution. These surviving compact cores of star particles are still recognized by SUBFIND as self-bound structures, and give rise to the low-mass extension of the subhalo mass functions. The flattening of the mass function in these regimes shows that the number of DM-poor galaxies is affected by the finite numerical resolution.

The right-hand panel of Fig. 4 shows the subhalo mass functions of just the stellar component, for the different radiative runs. As expected, the effect of changing the feedback strength is now clearly visible and can lead to nearly a factor of 10 in stellar mass between simulations without kinetic feedback (CSFNW) and with strong kinetic feedback (CSFSW; see also Saro et al. 2006). This comparison highlights the existing interplay between the feedback, which regulates the star-formation within subhaloes and its progenitor haloes, and the stripping due to the highly pressurised environment of the ICM. Although thermal conduction is expected to alter the efficiency of gas stripping (e.g. Price 2008), its low efficiency in the low-temperature subhaloes results only in a marginal impact on the resulting stellar mass function. In Appendix A, we will further examine the numerical convergence of the stellar mass function of the cluster galaxies.

In Fig. 6, we consider the time evolution of the subhalo mass functions by showing averages for the main progenitors of the eight high-mass clusters at different redshifts. For the DM-only simulations, we do not see any significant evolution over the considered redshift range. This is not directly in contrast to findings by Gao et al. (2004), as they define the virial mass with respect to 200 times the critical density. If we stick to the same definition of virial mass and radius, we also get a evolutionary trend in the same direction than found in Gao et al. (2004). The analysis of the average subhalo mass function over the full sample of massive clusters confirms the effect of the gas stripping in the non-radiative runs, already discussed for the *g51* cluster at $z = 0$, and the counteracting effects by cooling and star-formation in the radiative runs.

Furthermore, the rightmost upper and lower panels show the results at $z = 0$ and 1, respectively. At intermediate subhalo mass (between 10^{11} and $10^{12}\,M_{\odot}$), the effects of cooling and star formation are that of slightly increasing the subhalo mass function compared with the pure DM run. This is especially true at high redshift, when stripping is less efficient. There are indications that, at the high-mass end, stripping can still be efficient enough to suppress the subhalo mass function, also in the runs with cooling and star formation. Again, a measurable effect is seen from star-dominated substructures for the low-mass subhaloes, indicating that clumps of star particles, being more compact than DM subhaloes, are more resistant against tidal destruction. However, even the radiative simulations do not predict that a significant fraction of galaxies without DM haloes survive down to $z = 0$.

Fig. 7 shows the evolution of the parameters of the power-law fit to the total subhalo mass function, where we have as usual restricted the fitting range to haloes with at least 100 DM particles and $m_{\rm sub}/M_{\rm vir} < 0.01$, which gives a reasonable fit over the whole considered redshift range. To guarantee robust fits, we here excluded those haloes for which there are less than 20 data points in

Downloaded from https://academic.oup.com/mnras/article/399/2/497/1058378 by guest on 20 August 2022

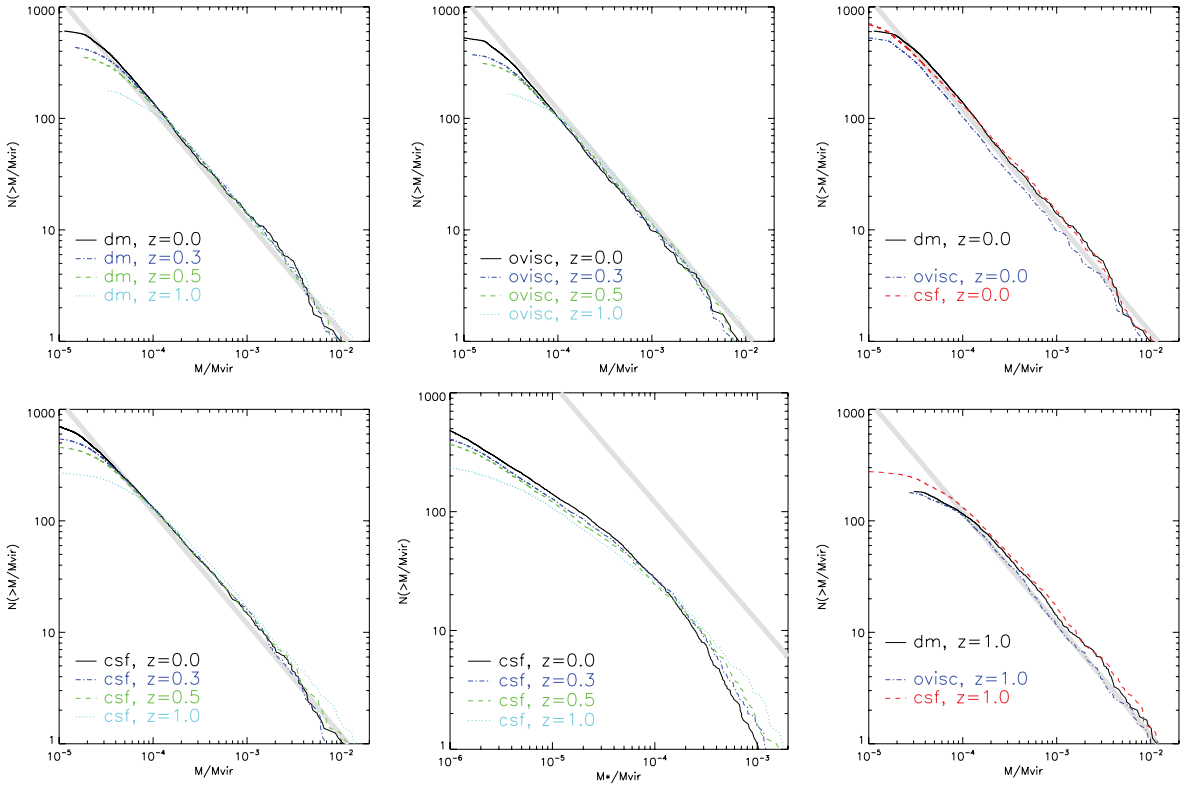

Figure 6. Evolution of the subhalo mass functions for the different runs, averaged over the eight clusters of the high-mass sample. The two left-hand and the two central panels show the mass functions at $z = 0, 0.3, 0.5$ and 1 with solid, dash–dotted, dashed and dotted lines, respectively. Upper-left, upper-central and lower-left panels are for total mass function for the DM, non-radiative *ovisc* and radiative *csf* runs, respectively. The lower central panel is for the stellar mass function of the radiative *csf* runs. The two right-hand panels compare the total mass function for DM, *ovisc* and *csf* runs at $z = 0$ (upper-right panel) and at $z = 1$ (lower-right panel). The thick grey lines in all panels mark the slope -1.

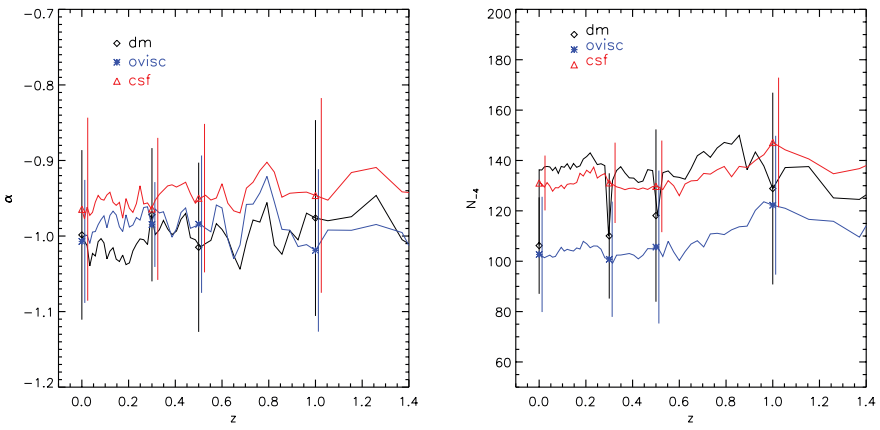

Figure 7. The evolution of the parameters defining the power-law shape of the subhalo mass function (see equation 1) for the progenitors of the eight clusters belonging to the high-mass subsample. All the 52 outputs of the simulations out to $z = 1.4$ have been used to produce the continuous lines. Different colours/symbols are for the DM runs, for the (OVISC) non-radiative run and for the (CSF) radiative runs. Left- and the right-hand panels show the evolution of slope and normalization, respectively. The error bars mark the rms scatter computed over the eight clusters of the high-mass subsample. For reasons of clarity, they are shown along with the symbols only at $z = 0, 0.3, 0.5$ and 1.0, and are slightly displaced in the horizontal direction.

the estimate of the cumulative mass function over this range. The slope of the total subhalo mass function does not show a significant evolution in all the runs. As for the normalization (right-hand panel of Fig. 7), its value for the non-radiative (OVISC) gas run is always below that of the DM and of the radiative CSF gas runs. There is also an indication that the radiative run at high redshift has a normalization slightly higher than the DM run. The stripping of the gas in the non-radiative run is relatively independent of the halo mass, thus leading to a slope similar to that of the DM case. We note that there is a tentative indication that the condensation of baryonic matter at the centre of the substructures in radiative runs leads to a small systematic trend with redshift, leading to a slightly flatter subhalo mass function at early redshift in the CSF runs.

© 2009 The Authors. Journal compilation © 2009 RAS, MNRAS **399,** 497–514

Downloaded from https://academic.oup.com/mnras/article/399/2/497/1058378 by guest on 20 August 2022

4.3 The composition of subhaloes

In DM-only simulations, it is known that tidal stripping induces strong radial dependences in the properties of substructures (e.g. De Lucia et al. 2004; Gao et al. 2004). For example, the substructure abundance is antibiased relative to the mass distribution of the cluster, and the average concentration of subhaloes increases towards the cluster centre. The efficiency of gas stripping from substructures also depends strongly on cluster-centric distance (see Gunn & Gott 1972; McCarthy et al. 2008), hence we expect radial variations in the relative content of baryons in subhaloes, which we analyse in this section.

The problem is made especially interesting by the complex non-linear interplay between the condensation of baryons due to radiative cooling, the gas-dynamical stripping processes and the resulting orbital evolution of affected subhaloes. Indeed, while gas stripping in the high-pressure ICM makes subhaloes more fragile, the formation of a compact core of cooled gas and stars makes subhaloes more resistant to disruption. As a result, we expect that the relative stellar content of a subhalo and its capability to retain a gaseous halo will depend both on the details of the physics included in the simulation and on its cluster-centric distance.

In order to investigate this in more detail, we show in Fig. 8 the radial dependence of the fraction of subhalo masses contributed by stars for the radiative runs including the reference kinetic feedback (*csf*), at various different epochs ($z = 0$, 0.3, 0.5, 1 and 2). Quite clearly, the stellar component becomes progressively more important in subhaloes found at a smaller cluster-centric distance. This is consistent with the expectation that the strong tidal interactions in the cluster central regions are efficient in removing the DM component of the subhaloes, while the gravitationally more tightly bound clumps of star particles are more resistant. Fig. 8 also shows that the radial dependence of the subhalo mass fraction in stars extends well beyond the clusters' virial radius $R_{\rm vir}$, thus indicating that the cluster environment affects the properties of the galaxy stellar population over a region much larger than the virial one (see also Saro et al. 2006). Note that a substantial fraction of these subhaloes detected at $r > R_{\rm vir}$ may have already crossed the cluster virial region in earlier passages and constitute the so-called 'backsplash population' (see Gill, Knebe & Gibson 2005; Ludlow et al. 2008). Their orbits have brought them into the outer parts again, with a fraction of them eventually destined to escape the cluster.

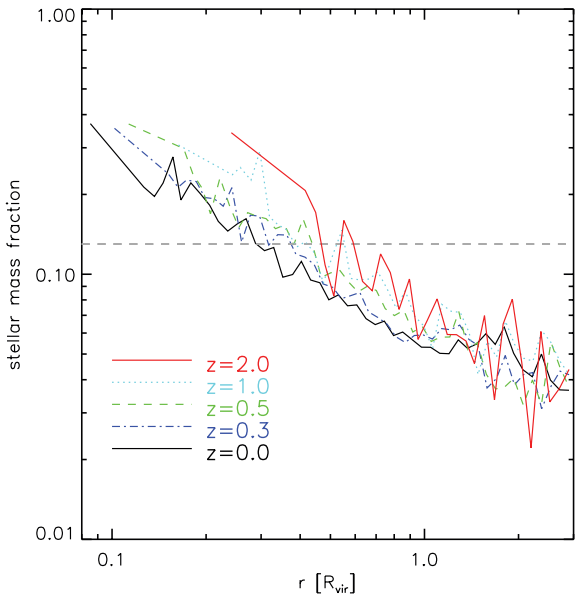

Figure 8. The evolution of the radial profiles of the stellar mass fraction within subhaloes for the radiative *csf* run. Each curve is obtained by averaging over the eight clusters belonging to the high-mass sample. Only subhaloes with masses $\leq 2 \times 10^{12}\,{\rm M}_{\odot}$ have been included in this analysis. The horizontal dashed line marks the cosmic baryon fraction assumed in our simulations.

Towards the centre of the clusters, the star fraction within subhaloes reaches values higher than the cosmic baryon fraction. At first glance, this result lends support to the assumption made by many SAMs of galaxy formation that galaxies can preserve their identity for a while even after their host DM haloes are destroyed by the tidal interaction within clusters (Gao et al. 2004). However, in SAMs (like De Lucia & Blaizot 2007) based on DM simulations of comparable resolution (like the *Millennium Run;* Springel et al. 2005) about half of the galaxies within the virial radius of the parent cluster are expected to have lost their DM haloes at $z = 0$, while in our hydrodynamical simulations we find that only $\approx$20 per cent of the galaxies have a star component which exceeds the mean cosmic baryon fraction (i.e. $m^{*}_{\rm sub} > 0.13\,m_{\rm sub}$), while only 2 per cent of the galaxies have their mass dominated by star particles (i.e. $m^{*}_{\rm sub} > 0.5\,m_{\rm sub}$). This implies that only a small fraction of our star-dominated systems can be classified as ORPHAN galaxies, which are defined as those galaxies not having a counterpart in the corresponding DM-only run. A precise comparison requires, however, a carefully matched magnitude selection, which is outside the scope of this paper. Future, yet higher resolution hydrodynamical simulations should in principle allow an accurate calibration of the SAM assumptions about the relative survival time of satellite galaxies once their parent DM halo cannot be tracked any more.

A related question concerns the ability of infalling subhaloes to retain a gravitationally bound component of diffuse gas during the cluster evolution. We show in Fig. 9 the cluster-centric dependence of the subhalo mass fraction associated with gravitationally bound gas (in units of the cosmic baryon fraction) from the set of eight massive clusters, at $z = 0$, 1 and 2. In each panel, we compare results for the OVISC non-radiative run with those for the radiative *csf* run. Furthermore, the solid lines indicate the radial dependence of the average subhalo gas mass fraction, which is computed by including also those subhaloes which do not have any gravitationally bound gas component. We indicate with the thin lines the Poisson uncertainties in the estimate of the average gas mass fraction, by assuming them to be proportional to the square root of the number of galaxies in each radial bin. At $z = 0$, we note that, whenever a subhalo retains a gas component, the associated mass fraction is higher in the non-radiative run than in the radiative one. This is related to the fact that a significant fraction of this gas is converted into stars in the radiative case.

On the other hand, the central concentration of star particles in subhaloes in the radiative runs makes them more resistant against ram pressure stripping. As a consequence, a larger number of subhaloes preserve a gas component, thus explaining the higher average gas fraction at all radii. Within the virial radius, we find at $z = 0$ that about $\simeq$1 per cent of the resolved subhaloes still have some self-bound gas, both in the OVISC and in the CSF runs, with a marginal indication for a smaller amount of gas in the CSF clusters, due to its conversion into stars. As expected, at high redshift ram pressure stripping has not yet been as effective, thus explaining the larger fraction of self-bound gas, which is $\simeq$4 and 6 per cent for the OVISC

Downloaded from https://academic.oup.com/mnras/article/399/2/497/1058378 by guest on 20 August 2022

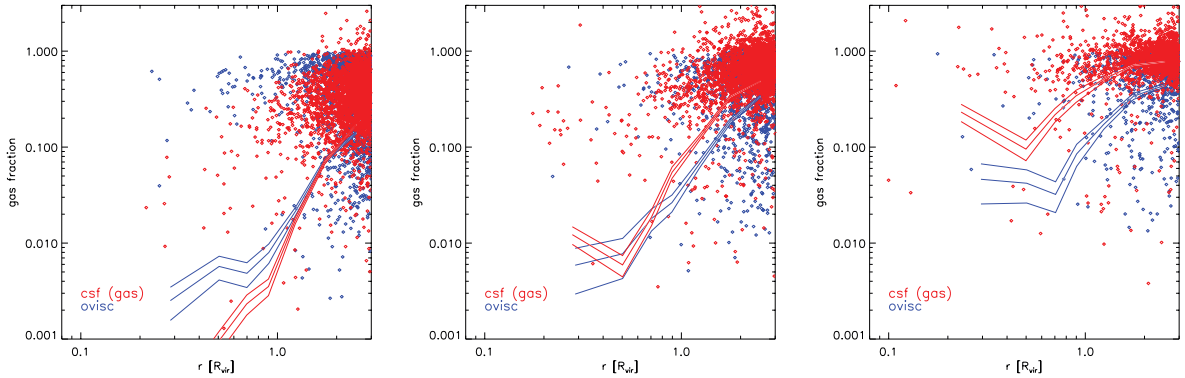

Figure 9. The radial dependence of the fraction of subhalo mass in gas, in units of the cosmic baryon fraction, for the eight clusters belonging to our high-mass sample. Black and blue symbols are for the subhaloes retaining a gravitationally bound gas component for the non-radiative *ovisc* and for the radiative *csf* runs, respectively. The heavy continuous lines show the radial dependence of the gas fraction after averaging over all subhaloes, including those not retaining any gas, while the light lines indicate the uncertainties arising from the small number statistics of the involved subhaloes. Left-hand, central and right-hand panels are for $z = 0$, 1 and 2, respectively.

and the CSF runs, respectively. Again, we note that the radial dependence of the gas fraction extends well beyond the virial radius, thus confirming that the overdense cluster environment affects the structure and evolution of subhaloes over a fairly large region surrounding the clusters (see also Dolag et al. 2006). Also note that at very high redshift the collapse of the gas due to efficient cooling inside the subhaloes can even lead to gas fractions larger than the cosmic values in the radiative runs.

An important question for hydrodynamical simulations of cosmic structure formation is how faithfully they are able to describe the gas-dynamical processes which determine the stripping of the gas in substructures moving in a high-density environment. In these processes, hydrodynamical fluid instabilities that are difficult to resolve can play an important role. In general, the faithfulness of the simulation depends both on the hydrodynamical scheme adopted (i.e. Eulerian or Lagrangian, implementation of gas viscosity, etc.) and on the numerical resolution achieved (e.g. Dolag et al. 2005; Sijacki & Springel 2006; Agertz et al. 2007; Iapichino & Niemeyer 2008). Although a detailed study of these numerical aspects is beyond the scope of this paper, it is interesting to examine the impact of the adopted artificial viscosity parameterization on the gas stripping from subhaloes.

Fig. 10 shows the subhalo gas mass fraction as a function of cluster-centric distance for the four clusters of our high-mass sample, for which runs with different artificial viscosities have been carried out (i.e. simulations *g1.a*, *g8.a*, *g51.a* and *g72.a*; see Table 2). Similarly to the results obtained by Dolag et al. (2005) for the predicted ICM turbulence, the OVISC and SVISC implementations give quite similar results, whereas the LVISC low-viscosity scheme leads to smaller gas-mass fractions inside the haloes and slightly higher gas-mass fractions outside the virial radius. This is a clear indication that numerical viscosity has a measurable effect on the stripping of gas from the subhaloes, as the latter depends on the environment.

The different behaviour of the lower viscosity scheme can be understood by recalling that this approach provides less efficient viscous stripping, which explains the larger gas fraction associated with subhaloes found in the cluster outskirts. On the other hand, as subhaloes cross the virial radius and enter a progressively more pressurized environment, they should experience hydrodynamical instabilities in the shear flows around the subhalo's gas, such as the Kelvin–Helmholtz instability, which may be poorly represented in SPH (Agertz et al. 2007). While the low-viscosity scheme does not improve the SPH description to a point where these instabilities are captured satisfactorily with SPH, it still improves the description of shear flows, so that the subhalo gas can be dissolved and dispersed in the hotter atmosphere over a relatively short timescale.

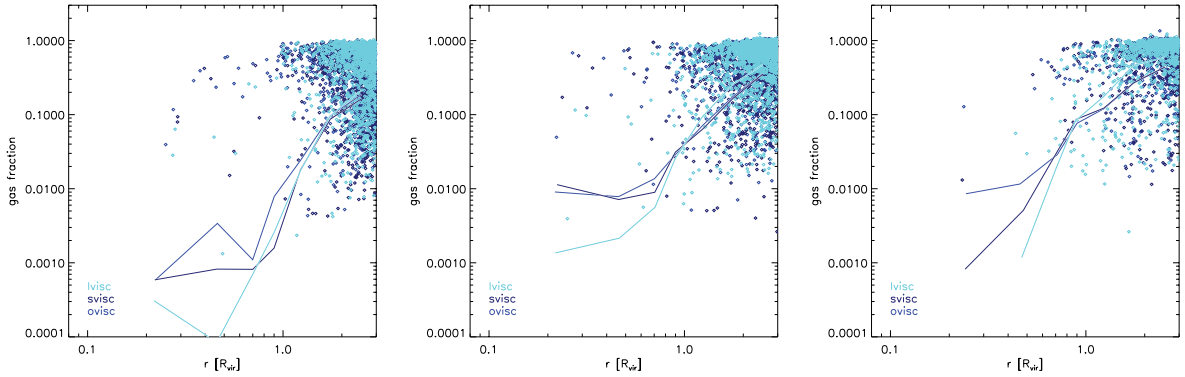

Figure 10. The same as in Fig. 9, but comparing results for the different implementation of artificial viscosity. Results are shown for the four clusters of the high-mass sample for which runs with the different viscosity schemes have been carried out.

Downloaded from https://academic.oup.com/mnras/article/399/2/497/1058378 by guest on 20 August 2022

5 CONCLUSIONS

In this study, we presented an analysis of the basic substructure properties in high-resolution hydrodynamical simulations of galaxy clusters carried out with the TREEPM–SPH code GADGET. We used a fairly large set of 25 clusters, with virial masses in the range 1–$33 \times 10^{14}\,h^{-1}\,\mathrm{M}_{\odot}$, out of which eight clusters have masses above $10^{15}\,h^{-1}\,\mathrm{M}_{\odot}$. The identification of the substructures has been carried out with the SUBFIND algorithm (Springel et al. 2001b), which we suitably modified to account for the presence of gas and star particles in hydrodynamical simulations. The primary aim of our analysis was to quantify the impact that gas physics has on the properties of subhaloes, especially on their abundance. Note that previous work has so far almost exclusively analysed substructures in DM-only simulations, so that our study is one of the first attempts to directly compare the DM-only results to those of hydrodynamical simulations that also account for baryonic physics.

We analysed non-radiative hydrodynamical simulations as well as radiative simulations, including star formation and different efficiencies for energy feedback associated with galactic outflows. Also, we examined the sensitivity of our results with respect to different parameterizations for the artificial viscosity needed in SPH. The main results of our analysis can be summarized as follows.

(i) Consistent with previous studies (Springel et al. 2001b; De Lucia et al. 2004), we find that the subhalo mass function in DM-only runs converges well for different numerical resolution over the mass range where substructures are resolved with at least $\simeq$30 gravitationally bound DM particles. We extend this result to show that the same convergence also holds well for the total subhalo mass function in hydrodynamical runs, irrespective of whether cooling and star formation are included in the simulations.

(ii) In non-radiative hydrodynamical simulations, the presence of a gas component leads to a reduction of the total subhalo mass function with respect to DM-only runs. On average, the reduction in mass of the substructures is *slightly* larger than expected from the complete stripping of the baryonic component. *This* is due to a combination of the modification of the subhalo orbits arising from the pressure force exerted by the ICM. *Furthermore, we see indications for an* increased susceptibility of the surviving DM haloes to tidal disruption.

(iii) In general, we find that only a very small fraction of subhaloes, of order of 1 per cent, within the cluster virial radii maintain a self-bound atmosphere of hot gas. This indicates a high efficiency for the stripping of the hot gas component in our simulations. The radial dependence of the mean gas fraction within subhaloes indicates that gas stripping starts already at large cluster-centric distances, beyond the virial radius. Using a scheme for reduced artificial viscosity has the effect of reducing viscous stripping in the cluster periphery, while increasing the stripping within the virialized high-density region.

(iv) In radiative runs that include star formation, some of the baryons are protected from stripping due to their concentration at the centres of the subhaloes. In this case, substructures have masses which are comparable to, or are slightly larger than in the DM-only runs. The stellar mass fraction is also found to strongly increase for subhaloes close to the centre. This confirms that compact clumps of star particles are indeed more resistant against tidal destruction than DM subhaloes. Despite this, we find that only a small fraction of subhaloes are dominated by their stellar component. As a result, the number of star-dominated galaxies is smaller than expected when, like usually assumed in SAMs of galaxy formation, they are allowed to survive for a dynamical friction time after the disruption of their DM halo. This suggests that our hydrodynamical simulations at their current resolution may not be able yet to accurately follow the survival of galaxies within clusters after the destruction of their DM subhaloes.

Our study shows that the technical improvements we implemented in SUBFIND allow a reliable identification of substructures in hydrodynamical simulations that include radiative cooling and star formation. This allows a direct identification of satellite galaxies not only in clusters of galaxies but also in future high-resolution hydrodynamical simulations of galaxy-sized haloes. This is essential to make direct contact with observational data, and also allows studies of the structural impact of baryonic physics on substructure. As our result show here, gas physics *does alter* substructure statistics in interesting ways, but the effects depend on physical processes such as radiative cooling and feedback. This also means that the approximate self-similarity of substructure properties that has been found in DM-only simulations of clusters and galaxy-sized objects (Moore et al. 1999) is not expected to hold nearly as well in simulations with radiative cooling. For example, in galaxy-sized haloes, many subhaloes will be so small that they do not experience atomic cooling; as a result, their behaviour should be close to our non-radiative results, and we would here expect a reduction of their abundance relative to the DM-only case.

In future work, it will be important to further improve the numerical description and resolution of our simulations, in order to be able to more accurately follow in particular the star-dominated substructures (i.e. galaxies) within galaxy clusters. This will then also provide important input for the SAMs of galaxy formation, allowing a check and calibration of their dynamical friction and gas stripping prescriptions.

ACKNOWLEDGMENTS

We thank an anonymous referee for constructive comments which helped to improve the presentation of the results. The simulations were carried out on the IBM-SP4 machine at the 'Centro Interuniversitario del Nord-Est per il Calcolo Elettronico (CINECA, Bologna)', with CPU time assigned under an INAF-CINECA grant, on the IBM-SP3 at the Italian Centre of Excellence 'Science and Applications of Advanced Computational Paradigms', Padova and on the IBM-SP4 machine at the 'Rechenzentrum der Max-Planck-Gesellschaft' at the 'Max-Planck-Institut für Plasmaphysik' with CPU time assigned to the 'Max-Planck-Institut für Astrophysik'. KD acknowledges the hospitality of the Department of Astronomy of the University of Trieste and the receipt of a 'Short Visit Grant' from the European Science Foundation for the activity entitled 'Computational Astrophysics and Cosmology'. We thank Gerard Lemson for all the support with the data base and related issues. We also thank Gabriella De Lucia and Alex Saro for a number of useful discussions. This work has been partially supported by the PD51 INFN Grant, by the ASI-COFIS and by the ASI-AAE contracts.

REFERENCES

Abadi M. G., Moore B., Bower R. G., 1999, MNRAS, 308, 947
Agertz O. et al., 2007, MNRAS, 380, 963
Ameglio S., Borgani S., Diaferio A., Dolag K., 2006, MNRAS, 369, 1459
Ameglio S., Borgani S., Pierpaoli E., Dolag K., 2007, MNRAS, 382, 397
Balsara D. S., 1995, J. Comput. Phys., 121, 357
Baugh C. M., 2006, Rep. Prog. Phys., 69, 3101
Bonaldi A., Tormen G., Dolag K., Moscardini L., 2007, MNRAS, 378, 1248
Borgani S. et al., 2004, MNRAS, 348, 1078

Downloaded from https://academic.oup.com/mnras/article/399/2/497/1058378 by guest on 20 August 2022

Borgani S. et al., 2006, MNRAS, 367, 1641
Borgani S., Diaferio A., Dolag K., Schindler S., 2008, Space Sci. Rev., 134, 269
Cora S. A., Tornatore L., Tozzi P., Dolag K., 2008, MNRAS, 386, 96
De Lucia G., Blaizot J., 2007, MNRAS, 375, 2
De Lucia G., Kauffmann G., Springel V., White S. D. M., Lanzoni B., Stoehr F., Tormen G., Yoshida N., 2004, MNRAS, 348, 333
Diemand J., Moore B., Stadel J., 2004, MNRAS, 352, 535
Dolag K., Bartelmann M., Perrotta F., Baccigalupi C., Moscardini L., Meneghetti M., Tormen G., 2004a, A&A, 416, 853
Dolag K., Jubelgas M., Springel V., Borgani S., Rasia E., 2004b, ApJ, 606, L97
Dolag K., Vazza F., Brunetti G., Tormen G., 2005, MNRAS, 364, 753
Dolag K., Meneghetti M., Moscardini L., Rasia E., Bonaldi A., 2006, MNRAS, 370, 656
Dolag K., Reinecke M., Gheller C., Imboden S. 2008, New J. Phys., 10, 125006
Dunkley J. et al., 2009, ApJS, 180, 306
Eke V. R., Cole S., Frenk C. S., 1996, MNRAS, 282, 263
Ettori S., Dolag K., Borgani S., Murante G., 2006, MNRAS, 365, 1021
Gao L., De Lucia G., White S. D. M., Jenkins A., 2004, MNRAS, 352, L1
Ghigna S., Moore B., Governato F., Lake G., Quinn T., Stadel J., 2000, ApJ, 544, 616
Gill S. P. D., Knebe A., Gibson B. K., 2005, MNRAS, 356, 1327
Giocoli C., Tormen G., van den Bosch F. C., 2008, MNRAS, 386, 2135
Gnedin O. Y., Kravtsov A. V., Klypin A. A., Nagai D., 2004, ApJ, 616, 16
Górski K. M., Hivon E., Wandelt B. D., 1998, in Banday A. J., Sheth R. K., Da Costa L., eds, Proc. MPA/ESO Conf., Evolution of Large-Scale Structure: From Recombination to Garching (astro-ph/9812350)
Gunn J. E., Gott J. R. I., 1972, ApJ, 176, 1
Haardt F., Madau P., 1996, ApJ, 461, 20
Iapichino L., Niemeyer J. C., 2008, MNRAS, 388, 1089
Jubelgas M., Springel V., Dolag K., 2004, MNRAS, 351, 423
Kenney J. D. P., van Gorkom J. H., Vollmer B., 2004, AJ, 127, 3361
Komatsu E. et al., 2009, ApJS, 180, 330
Kravtsov A. V., Berlind A. A., Wechsler R. H., Klypin A. A., Gottlöber S., Allgood B., Primack J. R., 2004, ApJ, 609, 35
Lemson G., Virgo Consortium T., 2006, preprint (astro-ph/0608019)
Lin W. P., Jing Y. P., Mao S., Gao L., McCarthy I. G., 2006, ApJ, 651, 636
Ludlow A. D., Navarro J. F., Springel V., Jenkins A., Frenk C. S., Helmi A., 2009, ApJ, 692, 931
Macciò A. V., Moore B., Stadel J., Diemand J., 2006, MNRAS, 366, 1529
McCarthy I. G., Frenk C. S., Font A. S., Lacey C. G., Bower R. G., Mitchell N. L., Balogh M. L., Theuns T., 2008, MNRAS, 383, 593
Meneghetti M., Argazzi R., Pace F., Moscardini L., Dolag K., Bartelmann M., Li G., Oguri M., 2007, A&A, 461, 25
Meneghetti M. et al., 2008, A&A, 482, 403
Monaghan J. J., 1997, J. Comput. Phys., 136, 298
Monaghan J. J., Gingold R. A., 1983, J. Comput. Phys., 52, 374
Moore B., Ghigna S., Governato F., Lake G., Quinn T., Stadel J., Tozzi P., 1999, ApJ, 524, L19
Morris J. P., Monaghan J. J., 1997, J. Comput. Phys., 136, 41
Murante G., Giovalli M., Gerhard O., Arnaboldi M., Borgani S., Dolag K., 2007, MNRAS, 377, 2
Nagai D., Kravtsov A. V., 2005, ApJ, 618, 557
Navarro J. F., Frenk C. S., White S. D. M., 1996, ApJ, 462, 563
Price D. J., 2008, J. Comput. Phys., 227, 10040
Puchwein E., Bartelmann M., 2006, A&A, 455, 791
Puchwein E., Bartelmann M., 2007, A&A, 474, 745
Puchwein E., Bartelmann M., Dolag K., Meneghetti M., 2005, A&A, 442, 405
Rasia E., Tormen G., Moscardini L., 2004, MNRAS, 351, 237
Rasia E., Mazzotta P., Borgani S., Moscardini L., Dolag K., Tormen G., Diaferio A., Murante G., 2005, ApJ, 618, L1
Rasia E. et al., 2006, MNRAS, 369, 2013
Salpeter E. E., 1955, ApJ, 121, 161
Saro A., Borgani S., Tornatore L., Dolag K., Murante G., Biviano A., Calura F., Charlot S., 2006, MNRAS, 373, 397
Saro A., De Lucia G., Dolag K., Borgani S. 2008, MNRAS, 391, 565
Sijacki D., Springel V., 2006, MNRAS, 371, 1025
Springel V., 2005, MNRAS, 364, 1105
Springel V., Hernquist L., 2002, MNRAS, 333, 649
Springel V., Hernquist L., 2003, MNRAS, 339, 289
Springel V., White M., Hernquist L., 2001a, ApJ, 549, 681
Springel V., White S. D. M., Tormen G., Kauffmann G., 2001b, MNRAS, 328, 726
Springel V. et al., 2005, Nat, 435, 629
Springel V., Frenk C. S., White S. D. M., 2006, Nat, 440, 1137
Stadel J. G., 2001, PhD thesis, Univ. Washington
Steinmetz M., White S. D. M., 1997, MNRAS, 288, 545
Stoehr F., White S. D. M., Tormen G., Springel V., 2002, MNRAS, 335, L84
Stoehr F., White S. D. M., Springel V., Tormen G., Yoshida N., 2003, MNRAS, 345, 1313
Tormen G., Bouchet F. R., White S. D. M., 1997, MNRAS, 286, 865
Tormen G., Moscardini L., Yoshida N., 2004, MNRAS, 350, 1397
Vazza F., Tormen G., Cassano R., Brunetti G., Dolag K., 2006, MNRAS, 369, L14
Weinberg D. H., Colombi S., Davé R., Katz N., 2008, ApJ, 678, 6
White S. D. M., 1996, in Schaeffer R., Silk J., Spiro M., Zinn-Justin J., eds, Proc. Les Houches Summer School, Cosmology and Large Scale Structure Formation and Evolution of Galaxies. Elsevier, Amsterdam, p. 349
Yoshida N., Sheth R. K., Diaferio A., 2001, MNRAS, 328, 669

APPENDIX A: NUMERICAL STABILITY

This appendix is devoted to a discussion of the numerical stability of the results presented for the properties of the substructures in simulated clusters. In the first part, we will discuss the robustness of the results against the choice of the subhalo-finding algorithm. In the second part, we will discuss the stability of the subhaloes mass functions against numerical resolution, choice of the minimum SPH smoothing length and scheme to add gas particles to initial conditions.

A1 Substructure detection

In Section 3, we described our modification of the SUBFIND algorithm (Springel et al. 2001b) to allow a clear detection of substructures with various compositions in hydrodynamical simulations including cooling and star formation. To verify our method, we reanalysed some of the clusters studied in Murante et al. (2007) with the new method and compared the identified stellar components of the individual galaxies. Note that the identification of galaxies in Murante et al. (2007) was based on a completely independent method, namely {SKID} (Stadel 2001). Note that SKID works best if applied only on the distribution of star particles. Therefore, for the sake of comparison, we excluded from our SUBFIND galaxies those having no stellar component.

Fig. A1 shows a comparison for the *R3* run of the positions, individual masses and stellar subhalo mass functions. We find an excellent agreement between the stellar masses inferred from both algorithms; in fact, the majority are identical for both algorithms. Only for the very loosely bound star particles at the periphery of the substructures some differences occur. The middle panel of the figure shows a comparison between the stellar masses of the galaxies identified by the two algorithms. Note that the horizontal and the vertical branches at low masses indicate the galaxies which are identified by one of the two algorithms. However, it is worth mentioning that there is no indication of any systematic offset between the results, and most of the scatter arises because sometimes

Downloaded from https://academic.oup.com/mnras/article/399/2/497/1058378 by guest on 20 August 2022

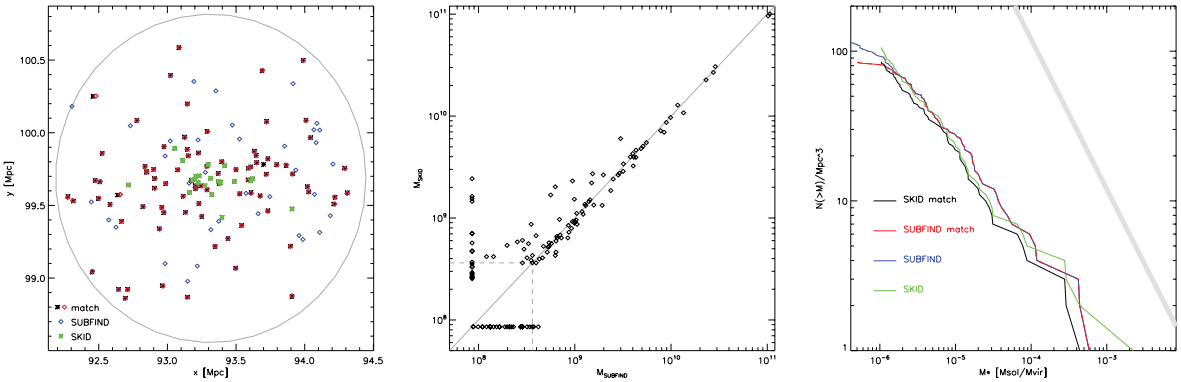

Figure A1. Comparison of the galaxies detected by SKID and by SUBFIND for the R3 run at $z = 0$. Left-hand panel shows the position of the individual substructures, with different symbols/colours for galaxies identified with the two algorithms, as specified in the labels. Red diamonds and black crosses indicate galaxies identified by SUBFIND and SKID, respectively, when the positions provided by the two algorithms differ by less than the half-mass radius of the galaxy in the SUBFIND identification. Blue diamonds and green crosses are for the galaxies identified by SUBFIND and SKID, respectively, when they do not have a counterpart identified by the other algorithm. In the results from SUBFIND, we do not include identified substructures which do not have a stellar component. The middle panel shows a one-to-one comparison between the stellar masses assigned by the two algorithms to the identified galaxies. The symbols lining up vertically/horizontally are those identified by one algorithm, but with no match in the galaxy sample from the other algorithm. The dashed lines mark the stellar mass limit applied to the SKID detection. Right-hand panel shows the cumulative stellar subhalo mass function from the two identification schemes. We also plot the mass functions for the galaxies identified from one algorithm and having a match in the galaxy sample derived from the other algorithm.

merging substructures get split into two parts only by one of the two algorithms. In this respect, we find that SUBFIND is marginally more efficient in separating two merging substructures. As a general result of our comparison, we conclude that our modifications of the SUBFIND algorithm are able to reliably identify the stellar parts of subhaloes even though we apply the substructure finder to all the particles in the simulations.

A2 Resolution and convergence

To test our results we performed several DM-only runs by a changing a number of parameters defining the numerical setup. Among the tests carried out, we mention the following: (i) use only the TREE-based gravity solver and compare with the TREEPM scheme; (ii) increase the accuracy of time integration and force computation far beyond the usual values assumed in our runs and (iii) change from $z = 5$ to 2 the redshift at which the gravitational softening switches from physical to comoving units. In all these tests, we verified that the subhalo mass functions do not show appreciable variations down to the mass corresponding to 20 self-bound DM particles.

As already discussed in Section 4.1, increasing resolution in the DM runs produces numerically stable results in the subhalo mass function, at least as long as only structures with at least 20 gravitationally bound DM particles are selected. The situation is expected to be different when considering instead hydrodynamical simulations, which include physical processes that are expected to be much more resolution dependent. The clearest example is radiative cooling, whose efficiency is known to depend on the mass resolution in cosmological simulations. In a similar fashion, hydrodynamical processes, such as ram pressure and viscous stripping, depend quite sensitively on the resolution adopted.

In order to assess the effect of resolution on the subhalo mass function, we carried out several simulations of a moderately poor clusters, having a virial mass $M_{\rm vir} \simeq 2.3 \times 10^{14}\,{\rm M}_{\odot}$. The setup of the initial conditions of this cluster have been described by Borgani et al. (2006) (it corresponds to the CL4 cluster of that paper). The cosmological model assumed in this case is the same as that for the sample of clusters analysed in this paper, except that a lower normalization $\sigma_8 = 0.8$ of the power spectrum was assumed (Borgani et al. 2004). Radiative simulations of this cluster have been carried out by varying the effective resolution in three different ways.

Table A1. The masses of the different particle species for the runs at different resolution.

Run	$m_{\rm dm}$	$m_{\rm gas}$	m_*	$M_{\rm sub}$	$T_{\rm CPU}$	System (GHz)
R1	2.2*e*9	3.3*e*8	1.7*e*8	1*e*11	55	OPTERON 2.8
R2	6.6*e*8	9.9*e*7	4.9*e*7	5*e*10	173	OPTERON 2.8
R3	1.5*e*8	2.2*e*7	1.1*e*7	<1*e*10	6126	POWER4 1.3
R2-8	6.6*e*8	7.9*e*8	4.0*e*8	7*e*10	63	OPTERON 2.8
R3-8	1.5*e*8	1.8*e*8	8.8*e*7	2*e*10	257	OPTERON 2.8

Note. Column 1: run name. Columns 2-4: masses of the DM, gas and star particles, respectively (in units of $\rm M_{\odot}$). Column 5: estimate of the stellar subhalo mass at which the simulations is numerically converged (since no higher resolution that R3 is achieved, we give only an upper limit in this case). Column 6: the CPU time (in hours) needed to perform the run.

(i) Increase the mass resolution by a factor of 4 and 15 with respect to a reference resolution. The corresponding force resolutions are decreased by a factor $4^{1/3}$ and $15^{1/3}$, respectively (runs R1, R2 and R3 in Table A1).

(ii) Change the criterion to assign gas particles in the initial conditions. Instead of using the same number of gas and DM particles, with a mass ratio reflecting the cosmic baryon fraction, we assigned one gas particle to every group of eight DM particles. In this way, the mass of each parent DM particle is decreased by an amount so as to reproduce the cosmic baryon fraction. Given the standard values of the cosmic baryon fraction, this procedure gives comparable masses to DM and gas particles, thus reducing a possible spurious numerical heating of the gas particles induced by two-body encounters with DM particles. This scheme of adding gas to initial conditions can be seen as a way of increasing the accuracy of the gravity part (i.e. increasing the number of DM particles) for a fixed resolution in the hydrodynamics. This prescription was originally suggested by Steinmetz & White (1997) as a computationally efficient way of suppressing two-body heating in cooling flows.

Downloaded from https://academic.oup.com/mnras/article/399/2/497/1058378 by guest on 20 August 2022

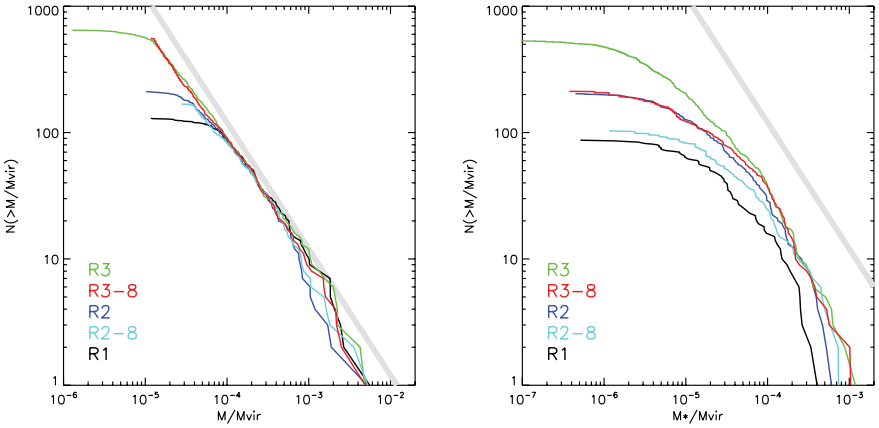

Figure A2. Comparison of the total (left-hand panel) and stellar (right-hand panel) subhalo mass functions, for runs with increasing resolution as well as for runs with the alternative 'gasification' scheme (see the text for details). Whereas the total subhalo mass function seems to be converged for subhaloes which are resolved by 30–50 DM particles, the stellar subhalo mass function appears to converge only much more slowly. Here, the one over eight gasification scheme seems to work better, because it converges earlier for fewer gas particles and only mildly more DM particles.

(iii) Use different values for the minimum SPH kernel smoothing length, in units of the gravitational softening, $h_{\rm sm}$. The choice of this smoothing length is somewhat arbitrary. In radiative simulations, cooling causes gas to collapse and form high-density cores at the centre of haloes, thus causing the SPH smoothing length of cooled gas particles to fall below the gravitational softening. One therefore often restricts the SPH smoothing length to a certain fraction of the gravitational softening, ranging between 0 (no restriction) and 1 (restricted to the gravitational softening). While the reference value adopted for our simulations is $h_{\rm sm} = 0.1$, we have tested the effect of increasing it up to a value of unity.

To separate the effects of numerics from those related to the physics included in the simulations, we decided to perform our study of numerical stability for the simplest version of the radiative runs, i.e. by not using the kinetic feedback associated with galactic winds (CSFNW runs).

In the left-hand panel of Fig. A2, we show the results of our resolution study. They confirm that the mass range over which the total subhalo mass function is reliably described widens from the R1 to the R3 run. In general, runs at varying resolution provide similar results at masses corresponding to at least 20 DM particles, thus confirming the result shown in Fig. 3 for DM-only runs. Quite interestingly, the R2-8 and R3-8 runs, based on using equal masses for DM and gas particles, provide results virtually indistinguishable from the corresponding R2 and R3 runs over the whole mass range where the results are stable against resolution. This confirms that the total mass function is determined by the DM mass resolution and that a numerically converged total mass function can be obtained with the alternative way of 'gasifying' initial conditions at a lower computational cost (see Column 6 in Table A1).

The results are different for the stellar mass function, shown in the right-hand panel of Fig. A2. Since these simulations are not including an effective feedback scheme which is able to regulate star formation, it is not surprising that the subhalo mass function progressively increases without any sign of convergence with resolution. A more interesting result concerns instead the behaviour of the R2-8 and R3-8 runs. Despite the fact that these runs have a poorer gas mass resolution than the R1 and R2 runs, respectively, they produce a higher stellar subhalo mass function. For instance, the R3-8 run is consistent with the R3 run down to $1.5 \times 10^{10}\,{\rm M}_{\odot}$, whereas the R2 run converges on the R3 run only at $5 \times 10^{10}\,{\rm M}_{\odot}$. This result is achieved with an acceptable increase of the computational cost. This highlights that increasing the DM mass resolution is indeed an efficient way of increasing the accuracy in the

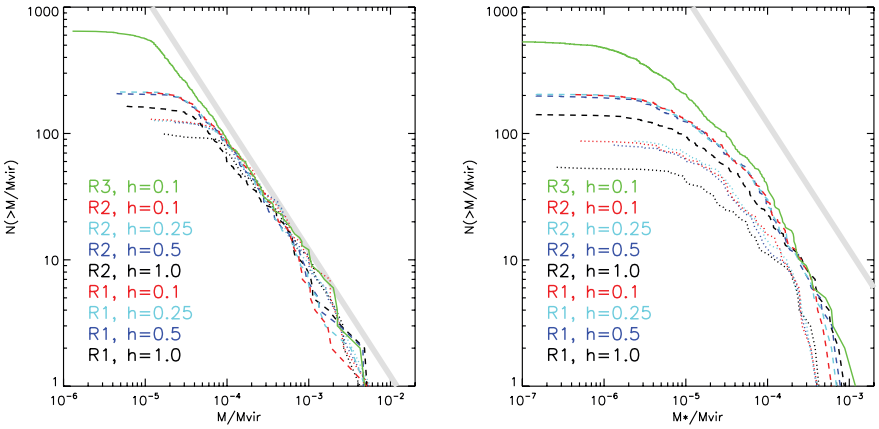

Figure A3. The total (left-hand panel) and stellar (right-hand panel) subhalo mass functions at different resolutions and using, at each resolution, different values for the minimum of the SPH smoothing length, $h_{\rm sm}$.

© 2009 The Authors. Journal compilation © 2009 RAS, MNRAS **399,** 497–514

Downloaded from https://academic.oup.com/mnras/article/399/2/497/1058378 by guest on 20 August 2022

description of cooling in small subhaloes, without overly increasing the CPU time requirements.

Finally, Fig. A3 shows the effect of changing the minimum value of the SPH smoothing length, $h_{\rm sm}$. As for the total subhalo mass function (right-hand panel), it has only a mild effect at the smallest resolved masses. We note that no differences exist for $h_{\rm sm} \leq 0.5$, while a significant reduction of the mass function takes place for $h_{\rm sm} = 1$. The effect is more apparent for the stellar mass function (left-hand panel). This result demonstrates that not allowing the SPH smoothing length to become smaller than the gravitational softening makes the star clumps more fragile within the strong tidal field of the cluster. We note that using a small $h_{\rm sm}$ is computationally cheaper, since it prevents the occurrence of computationally expensive SPH computations for a large number of neighbours in the highly dense regions of cold gas.

APPENDIX B: DATA BASE

The results of our substructure analysis for the *dm*, OVISC and CSF version of all our simulated clusters (with the exception of *g696*) are publicly available within the German Virtual Observatory. The access to the data is realized by a VO-oriented, SQL-queryable data base similar to the one described in Lemson & Virgo Consortium (2006). The web application that allows users to query the cluster data base (called *Hutt*) is located at {http://www.g-vo.org/HydroClusters}. Together with this publication, the data structures are made available to all users. The interface provides a full documentation of the available data and also gives different examples for scientific SQL queries, returning data which can be used to produce similar plots than presented in this paper. In the future, we plan to allow users to register and to build up their own data bases to store intermediate results from the queries to allow more complex analysis. Also, we plan to extend the underlying data base with further simulations that are not discussed in this study.

This paper has been typeset from a TEX/LATEX file prepared by the author.

Downloaded from https://academic.oup.com/mnras/article/399/2/497/1058378 by guest on 20 August 2022